Available online at www.sciencedirect.com
ScienceDirect
Journal of Computational Physics 226 (2007) 326–353
JOURNAL OF COMPUTATIONAL PHYSICS
www.elsevier.com/locate/jcp

Modeling diffusion in random heterogeneous media: Data-driven models, stochastic collocation and the variational multiscale method

Baskar Ganapathysubramanian, Nicholas Zabaras *

Materials Process Design and Control Laboratory, Sibley School of Mechanical and Aerospace Engineering, 188 Frank H.T., Rhodes Hall, Cornell University, Ithaca, NY 14853-3801, USA

Received 17 November 2006; received in revised form 21 March 2007; accepted 9 April 2007
Available online 24 April 2007

Abstract

In recent years, there has been intense interest in understanding various physical phenomena in random heterogeneous media. Any accurate description/simulation of a process in such media has to satisfactorily account for the twin issues of randomness as well as the multilength scale variations in the material properties. An accurate model of the material property variation in the system is an important prerequisite towards complete characterization of the system response. We propose a general methodology to construct a data-driven, reduced-order model to describe property variations in realistic heterogeneous media. This reduced-order model then serves as the input to the stochastic partial differential equation describing thermal diffusion through random heterogeneous media. A decoupled scheme is used to tackle the problems of stochasticity and multilength scale variations in properties. A sparse-grid collocation strategy is utilized to reduce the solution of the stochastic partial differential equation to a set of deterministic problems. A variational multiscale method with explicit subgrid modeling is used to solve these deterministic problems. An illustrative example using experimental data is provided to showcase the effectiveness of the proposed methodology.

Keywords: Stochastic partial differential equations; Random heterogeneous media; Microstructures; Collocation methods; Sparse grids; Multiscale modeling; Variational multiscale methods; Model reduction

1. Introduction

Thermal transport in random heterogeneous media is an ubiquitous process occurring in various scales ranging from the large scale (e.g. geothermal energy systems, geological heating of the earth's crust) to smaller scales (e.g. heat transfer through composites, blends, polycrystals, inter-dentritic diffusion and heat transfer through fluidized beds). In the past decade, there has been increasing interest in reliably modeling

* Corresponding author. Fax: +1 607 255 1222.
E-mail address: zabaras@cornell.edu (N. Zabaras).
URL: http://mpdc.mae.cornell.edu (N. Zabaras).

0021-9991/$ - see front matter
doi:10.1016/j.jcp.2007.04.009

and predicting the thermal behavior of such media. In this context, any realistic simulation and prediction methodology must satisfactorily deal with some important issues related with the property variation in random heterogeneous media:

- *Multiple length scales:* Properties like permeability and thermal conductivity exhibit variations across multiple length scales. This is because of the small scale variations in the microstructure of the media (change in phases, micro-porosity, holes and exclusions, cracks, etc.). These small scale variations in properties cannot be neglected as they usually result in considerable changes in the thermal behavior at the larger scales [1].
- *Statistical nature of properties:* It is not possible to experimentally determine the complete structure of the media at the finest scale. In most cases, only a few statistical properties of the structure are experimentally determined. These properties include the volume fraction, two-point correlations and three-point correlations among others. Every realization of the microstructure in the media will satisfy these correlations. This necessitates viewing the microstructure as a random field that satisfies certain statistical properties/correlations. As the thermophysical properties of the media implicitly depend on the microstructure, these properties must also be viewed as random fields.
- *Uncertainties in the system and properties:* Most physical models require some input constitutive relations and/or material properties. These inputs are usually available or derived from experimental data. The presence of uncertainties/perturbations in experimental studies implies that these input parameters have some inherent uncertainties. To accurately predict the performance of the system, it then becomes essential for one to include the effects of these input uncertainties into the model system and understand how they propagate and alter the final solution.

A brute force approach to assess the effects of the small scale variations would be to perform a fully-resolved transient computation. This computation requires spatial and temporal discretizations that would resolve the smallest length scales in the material data and the time scales in the solution. This methodology quickly becomes computationally intractable even for deterministic problems of moderate size. An alternate computational approach is to have a coarse-scale description that includes the small scale effects in an averaged form. Computational techniques have been developed that 'solve for a coarse-scale solution by defining an appropriate coarse-scale problem that captures the effect of the fine-scales' [2]. This is the central concept to most upscaling formulations. The more popular techniques developed for upscaling in the deterministic context fall under the category of multiscale methods viz. the variational multiscale (VMS) method (also known as operator upscaling) [3], the heterogenous multiscale method [4,5] and the multiscale finite element method [6]. These methods typically introduce multiscale basis functions at the coarse-scale. This essentially involves splitting the variational formulation for the governing equations into a coarse and a fine-scale part. The fine-scale part is then solved approximately to obtain the fine-scale solution model, that is substituted in the coarse-scale part of the variational formulation to obtain an upscaled problem. Further related techniques include the generalized finite element method [7] and residual-free bubbles [8].

Almost all of the above approaches have been exclusively limited to solving deterministic problems. The presence of uncertainties, either due to input uncertainties or formulating the microstructure as a random field, can be modeled in the system through reformulation of the governing equations as stochastic partial differential equations (SPDEs). A recent approach to model uncertainty is based on the spectral stochastic finite element method (SSFEM) [9]. In this method, the random field is discretized directly, i.e. uncertainty is treated as an additional dimension along with space and time and a field variable is expanded along the uncertain dimension using suitable expansions. The basic idea is to project the dependent variables of the model onto a stochastic space spanned by a set of complete orthogonal polynomials. This method has been applied with great success to investigate numerous physical phenomena [10–13]. Error bounds and convergence studies [14–16] have shown that these methods exhibit fast convergence rates with increasing orders of expansions. Though the SSFEM method has been used successfully in a variety of scenarios, it has a few drawbacks like the 'curse-of-dimensionality' and the intense programming effort required to build the framework (see [17–19] for a discussion). The SSFEM method cannot be easily applied to problems involving high stochastic dimension. It also cannot be easily extended to problems having steep gradients and discontinuities (there has been some recent progress in this regard, see [20]).

To solve problems in high-dimensional stochastic spaces and to allow non-smooth variations of the solution in the random space, there have been recent efforts to couple the fast convergence of the Galerkin methods with the decoupled nature of Monte Carlo sampling [21,22]. Xiu and Hesthaven [18], Xiu [19] and Nobile et al. [23] recently used the Smolyak algorithm to build sparse grid interpolants in high-dimensional space. Using this method, interpolation schemes (for the solution) can be constructed with orders of magnitude reduction in the number of sampled points to give the same level of approximation (up to a logarithmic factor) as interpolation on a uniform grid. Ganapathysubramanian and Zabaras [17] extended this methodology to adaptively sample more important dimensions, resulting in further computational gains. The sparse grid collocation and cubature schemes have been well studied and utilized in different fields [24–26].

Though the fields of multiscale modeling as well as stochastic modeling are relatively mature, there has not been much work on a combined stochastic, multiscale framework of analysis. To the best knowledge of the authors, the only previous work in this field is by Velamur Asokan and Zabaras [27], where a stochastic variational multiscale framework based on ideas from the generalized polynomial chaos expansion (GPCE) and VMS was developed. In [27], only the uncertainty in properties was considered with a fixed topology of the underlying two-phase medium. In a related work, Xiu and Tartakovsky [28] assumed that the random fluctuations in properties could be additively decomposed into a mean part and a fluctuating part. They used a coupled GPCE and random domain decomposition (RDD) methodology to solve for the stochastic variable. This methodology can be seen as a precursor to the multiscale methods. In the present work, an extension of the deterministic variational multiscale method (VMS) to include uncertainties that arise from random topology of the underlying medium is proposed. A sparse grid collocation strategy is utilized to construct the stochastic solution. The proposed methodology illustrates a general scheme to easily solve the twin problems of multilength scale variations in properties and the corresponding uncertainties associated with them.

In most analyses of diffusion through random heterogeneous media, the properties (property statistics) are usually assumed to be analytically known functions. Physically meaningful/useful solutions can be realized only if property statistics are experimentally obtained and used. Usually, experimental data regarding statistics and correlations of the microstructure (and properties) are known for the random heterogeneous media. We propose a methodology to utilize this experimentally available data to generate the stochastic inputs required in the stochastic variational multiscale (SVMS) framework. This is conceptually similar to the case of studies of flow in heterogeneous porous media (geological studies) where various techniques are used to reconstruct parameter fields from data. In the first step, a class of 3D microstructures, satisfying the experimental correlations, is reconstructed. A model reduction scheme (principle component analysis (PCA), Karhunun–Loève expansion (KLE)) is used to convert the infinite-dimensional space describing the class of microstructures to a finite-dimensional approximation of the space. The finite-dimensional model represents the class of allowable microstructures that satisfy the experimental correlations. This model is utilized as the stochastic input in the stochastic variational multiscale (SVMS) framework.

The proposed methodology seamlessly ties together three distinct aspects of realistic modelling of complex systems, namely (i) a general methodology for generating data-driven models of material and topological variations for use as stochastic inputs, (ii) a general decoupled methodology for accessing the effect of these input uncertainties on the complex system, and (iii) a multiscale methodology for upscaling the effects of fine scale features of the system. We would like to emphasize that there have been significant developments in each of the above three aspects of analysis individually. There have been advances in extracting stochastic models from experimental data [29]. Techniques like the random domain decomposition method [30–32], the maximum likelihood principle [33] and the maximum entropy principle [34,35] have been used to successfully reconstruct material models for use in stochastic analysis. There has been rapid developments in the analysis of multiple scales of property variations and towards extraction of useful (from an engineering context) coarse/large scale behavior [2,3,6]. Nevertheless, to the best knowledge of the authors, this is the first time that a robust methodology has been developed that seamlessly merges all these various aspects of analyses: from developing a data-driven model for generating inputs to a stochastic (multiscale) framework with an ultimate goal obtaining the probability distribution of the physical fields (e.g. temperature in a diffusion process) that arise from the randomness of the topology and properties of the underlying medium.

The layout of this article is as follows: in the next section, we introduce the problem of interest, with a discussion of the uncertainty in topology as well as the multilength scale variations in the topology. Section 3

describes the data-driven approach to generate the class of allowable microstructures given limited statistical microstructural information. A discussion of the techniques used to reduce this class of reconstructed microstructures into a finite-dimensional model is provided in Section 4. Section 5 describes the sparse-grid collocation methodology, while Section 6 describes the basics of the variational multiscale model used. Section 7 consists of an illustrative numerical example, wherein statistics of temperature variation in three-dimensions are constructed using an experimentally obtained two-dimensional microstructural image of a two-phase material. We conclude in Section 8 with some comments and avenues of future work.

2. Problem definition

The focus of this work is to investigate diffusion in heterogeneous media (henceforth referred to as the 'microstructure'). Fig. 1 shows three different kinds of such microstructures. Particular instances of diffusion through these microstructures could be heat flow through a pearlite structure, diffusion of sulphur through two-phase brass or the diffusion of contaminants through a soil specimen. The emphasis of this paper is on analyzing diffusion through such random microstructures.

Why is the microstructure random? The microstructure (as shown in Fig. 1) is typically obtained by experimentally visualizing a specific point (e.g. samples obtained from the surface of an extruded polycrystalline material or from a cast iron surface) in the specimen. If the microstructure were to be visualized at exactly the same point in another specimen (made from the same material and via the same process), one would expect to get a completely different image of the microstructure. It is only practical to experimentally take a finite number of samples of the microstructure, and usually all these microstructural images are different. Thus, if one were to consider any such specimen, the microstructure is inherently random (i.e. it is unknown) in that its topology varies from specimen to specimen. Even though the microstructural samples would be different, the topology of the microstructure satisfy some statistical properties as a result of the physical process path (e.g. extrusion, sintering) used to obtain the specimen. For instance, the volume fraction of one of the components in a two-phase microstructure is a first-order statistical property. All the microstructures should have the same volume fraction of the corresponding components, since they are obtained from the same material. Similarly, higher-order statistical properties involving the topology of the microstructures can be defined. Consequently, the microstructural topology can be considered as a random field (satisfying some statistical properties) and the microstructure in any arbitrary specimen is then a realization of this field. The thermal properties of the material obviously depend on the topology of the microstructure. We assume that the thermal properties of the material are uniquely defined by its microstructure (e.g. each point in a realization of a two-phase (α, β phases) medium is assumed to be uniquely occupied by one of the two phases and that each phase has given properties).

Remark 1. We will henceforth limit ourselves to a discussion of the microstructural topology. This will be used interchangeably to also mean the thermal property variation (i.e. the diffusivity, $\alpha = \frac{k}{\rho C_P}$) in the microstructure. When we state that the microstructure is random, we also mean that α is random.

The aim of the discussion above is to emphasize the fact that the microstructure and its thermal properties are not known explicitly since the underlying medium is only a realization of a random field. Only certain statistical moments of the microstructure and its properties are known. Let us denote these properties by $(P_1, \ldots, P_n)$. Any random microstructure that satisfies these statistical properties has a finite probability of

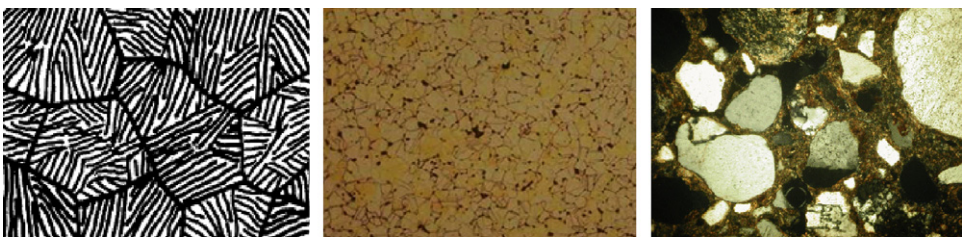

Fig. 1. Pictographs of three different heterogeneous microstructures: On the left: pearlite; In the middle: brass; On the right: soil.

being the microstructure. This statement can be stated rigourously as follows: Let Ω be the space of all microstructures that satisfy the statistical properties $(P_1, \ldots, P_n)$. This is our event space. Every point in this space is equiprobable. Consequently, we can define a σ-algebra $\mathscr{F}$ and a corresponding probability measure $\mathscr{P} : \mathscr{F} \to [0,1]$ to construct a complete probability space $(\Omega, \mathscr{F}, \mathscr{P})$ of allowable microstructures. The thermal properties of the random heterogeneous medium is represented as

$$\alpha(\boldsymbol{x}) = \alpha(\boldsymbol{x}, \omega), \quad \boldsymbol{x} \in D, \ \ \omega \in \Omega, \tag{1}$$

where $D \subset \mathbb{R}^d$ is the d-dimensional bounded domain that is associated with this medium. We re-iterate that the property randomness is assumed to be affiliated only with the topological variability of the microstructure. The governing equation for thermal diffusion in this medium is

$$\frac{\partial u(\boldsymbol{x}, t, \omega)}{\partial t} = \nabla \cdot [\alpha(\boldsymbol{x}, \omega) \nabla u(\boldsymbol{x}, t, \omega)] + f(\boldsymbol{x}, t, \omega), \quad \boldsymbol{x} \in D, \ \ t \in [0, T_f], \ \ \omega \in \Omega, \tag{2}$$

where u is the temperature and f is the thermal source/sink.

The variable u depends on the random field ω, which belongs to an infinite-dimensional probability space. The solution methodology is to first reduce the complexity of the problem by reducing the probability space into a finite-dimensional space. In most analysis, the random field $\alpha(\boldsymbol{x}, \omega)$ is assumed to be represented/described by a finite length random vector $[\xi^1, \ldots, \xi^N] : \Omega \to \mathbb{R}^N$. In other cases, the random field has a spatial correlation or variation and the 'finite-dimensional noise assumption' [15] ensures that the random field can be decomposed into a finite set of random variables. In the present case, the random field satisfies certain statistical properties $P_1, \ldots, P_n$. We utilize model reduction techniques like the Karhunen–Loève transform and principle component analysis to decompose the random field into a finite set of uncorrelated random variables (satisfying some bounds, see Section 4). Upon decomposition and characterization of the random inputs into N random variables, $\xi_i(\omega)$, $i = 1, \ldots, N$, the solution to the stochastic partial differential equation Eq. (2) can be written as

$$u(\boldsymbol{x}, t, \omega) = u(\boldsymbol{x}, t, \boldsymbol{\xi}), \quad \boldsymbol{\xi} = (\xi_1, \ldots, \xi_N), \tag{3}$$

where $\boldsymbol{\xi}$ is the N-tuple of the random variables. The domain of definition of $\boldsymbol{\xi}$ is denoted by Γ. The diffusion equation Eq. (2) can now be written as

$$\frac{\partial u(\boldsymbol{x}, t, \boldsymbol{\xi})}{\partial t} = \nabla \cdot [\alpha(\boldsymbol{x}, \boldsymbol{\xi}) \nabla u(\boldsymbol{x}, t, \boldsymbol{\xi})] + f(\boldsymbol{x}, t, \boldsymbol{\xi}), \quad \boldsymbol{x} \in D, \ \ t \in [0, T_f], \ \ \boldsymbol{\xi} \in \Gamma. \tag{4}$$

For the sake of brevity, we will denote the above system as $\mathscr{B}(u : \boldsymbol{x}, t, \boldsymbol{\xi}) = 0$.

Remark 2. We limit ourselves to a discussion of two-phase random microstructures. The proposed analytical developments can be extended to other types of microstructures in a straightforward manner.

Remark 3. Let L denote the length scales associated with the domain D. As discussed earlier the material making up this domain is highly heterogeneous. Its topology usually varies rapidly at a scale ϵ much smaller than the characteristic macro-length scale L ($\epsilon \ll L$). In the present work, we also look at computationally efficient methods to resolve the effect of these small scale variations in the topology.

The next two sections discuss the methodology to convert the given experimentally determined statistical properties $(P_1, \ldots, P_n)$ into a reduced-order finite-dimensional model for $\alpha(\boldsymbol{x},\omega)$. Then, computational techniques to reduce the effort required to resolve the effect of these small scale variations in the topology are formulated.

3. Data-driven reconstruction of the microstructure class

In order to construct a reduced-order finite-dimensional model for the stochastic microstructure in the material, it is necessary to first construct a database/library of possible microstructures. In the best case scenario, such a database already exists via experimental imaging of the microstructure across many different specimens. These images can then be used as instances of the microstructure. But such imaging procedures are both expensive and time-consuming to perform. Nevertheless, it has to be noted that such a procedure

would provide the most physically realistic database of microstructures. In most cases, the microstructure is imaged in a few specimens and certain statistical correlations are extracted. These experimentally determined correlations can be easily computed using simple image processing procedures. A brief description of the various experimentally useful correlations is provided next. This will also be useful in motivating the model reduction strategies developed in the next section.

3.1. Statistical correlation functions

Consider the digitized experimental image representing the random microstructure sampled at a point in the specimen. The two-phase random media consists of two disjoint regions of space: region $\mathscr{V}_1$ consists of phase 1, while region $\mathscr{V}_2$ consists of phase 2. The characteristic function or the indicator function for a particular phase, i is defined as

$$\begin{aligned} I^{(i)}(\boldsymbol{x}) &= 1, \quad \boldsymbol{x} \in \mathscr{V}_1, \\ &= 0, \quad \boldsymbol{x} \in \mathscr{V}_2. \end{aligned} \tag{5}$$

Volume fraction: The simplest statistical description of a random media is the volume fraction. The volume fraction can be interpreted in statistical terms as the probability of a point belonging to a phase [36,37]. This is the one-point correlation function defined as

$$\phi_1 = \langle I^{(1)}(\boldsymbol{x}) \rangle = \frac{1}{V} \int_V I^{(1)}(\boldsymbol{x}) \, \mathrm{d}\boldsymbol{x}. \tag{6}$$

Given a digitized image of the two-phase material, the volume fraction is just the number of phase 1 pixels by the total number of pixels in the image $\left(\phi_1 = \frac{1}{V} \int_V I^{(1)}(\boldsymbol{x}) \, \mathrm{d}\boldsymbol{x} = \frac{1}{N_{\text{pixels}}} \sum_{i=1}^{N_{\text{pixels}}} I^{(1)}(i) \right)$.

2-point correlation: A higher-order descriptor of the random media is the 2-point correlation. The 2-point correlation is defined as the probability that two randomly chosen points a distance r apart in the media, belong to the same phase i: $S_2^{(1)}(r) = \langle I^{(1)}(\boldsymbol{x}) I^{(1)}(\boldsymbol{x} + r\boldsymbol{e}_v) \rangle$, where $\boldsymbol{e}_v$ is a unit vector in an arbitrary direction v. In the integral form, $S_2^{(1)}(r) = \frac{1}{\Theta} \int_\Theta \frac{1}{V} \int_V I^{(1)}(\boldsymbol{x}) I^{(1)}(\boldsymbol{x} + r\boldsymbol{e}_v) \, \mathrm{d}\boldsymbol{x} \, \mathrm{d}v$, where $\boldsymbol{e}_v$ is a unit vector in the v direction, Θ is the range of variability of v (in two dimensions $\frac{1}{\Theta} \int_\Theta A \, \mathrm{d}v$ is $\frac{1}{2\pi} \int_0^{2\pi} A \, \mathrm{d}\theta$, while in three dimensions it is $\frac{1}{4\pi} \int_0^{2\pi} \int_0^{\pi} A \sin(\phi) \, \mathrm{d}\theta \, \mathrm{d}\phi$).

The discussion above enumerates few of the more important morphological characterizations of a random media. There are many more possible characterizations that provide other useful information about the random microstructures. These include the pore size distribution functions, surface correlation functions, cluster functions and nearest-neighbor functions. These characterizations can further be extended to multiphase, multicomponent systems. The interested reader is refereed to the excellent review on the subject by Torquato [36,38] and the references therein.

3.2. Reconstruction techniques

Given some experimentally determined statistical correlation functions of the random media, the goal is to reconstruct a large set of microstructures satisfying these correlation functions. This is the first step towards building a reduced-order model to the microstructural space. There are basically two ways of reconstructing microstructures: Statistics driven reconstruction and process driven reconstruction.

3.2.1. Statistics driven reconstruction

The reconstruction of random microstructures was first performed to obtain property bounds on elastic properties of materials [39]. There are various techniques for reconstructing random media from the given correlation functions:

- *Gaussian random fields and other models*: The microstructure is considered to be a level cut of a Gaussian random field (GRF). The statistical correlations are enforced during the construction of the GRF. This method has been shown to be very useful in describing porous materials, blends, polymers and ceramics.

Up to third-order correlation statistics have been used to reconstruct the random media [40–42]. Recent developments include multi-dimensional nonlinear transformations of Gaussian random fields to construct two-phase random media [43].

- *Simulated annealing and stochastic optimization:* These techniques construct an energy functional describing the microstructure. The energy of the microstructure represents its deviation from the required correlations functions. Various minimization techniques based on simulated annealing and stochastic optimization methods are used to minimize the energy leading to a microstructure that satisfies the correlation functions [39,44].
- *Maximum entropy methods*: A novel method of reconstructing the microstructure given limited statistical correlation functions is via posing the reconstruction problem as a maximum entropy problem [34,35,45]. Microstructures are assumed to be samples from a governing PDF and this PDF is computed using maximum entropy theory.

3.2.2. Process driven reconstruction

As stated at the beginning of the section, the best case scenario for model reduction would be a pre-existing database of microstructures via experimental imaging of the microstructure across many specimens. Instead of experimentally determining the microstructure, an alternative method to build the data set of possible microstructures is to directly simulate the thermo-mechanical process that results in these microstructures. This calculation of the microstructure from first principles becomes a computationally expensive problem. Nevertheless, these simulations can be done in small domains to make the process computationally feasible. Various examples of constructing a microstructure class via numerically simulating the evolution of the microstructure include Monte Carlo methods [46], phase field methods [35], as well as direct numerical simulation of microstructure evolution [47,48].

Remark 4. *Any* microstructure reconstruction technique can be utilized to construct realizations of the microstructure.

4. Model reduction

Following the schemes detailed in the previous section, it is straightforward to generate a large dataset of possible microstructures. This data set represents a set of unique points in the space of allowable microstructures. There are several dimension reduction schemes that are available to reduce this microstructural space into a finite-dimensional approximation. Principle component analysis is a powerful technique to obtain low-dimensional representation of a large amount of data. Using a set of large-dimensional data called the 'snapshots', the method decomposes the data into an optimal orthonormal basis. Few basis vectors selected in the order of importance can be used for the representation of the high-dimensional datasets. This method is well suited to the representation of microstructures.

Let the dataset contain M microstructures. Let us denote each of these images by I_i, $i = 1, \ldots, M$. Each image, I_i consists of $n \times n \times n$ pixels. The microstructure images are converted into M vectors ($X^{(i)}$) each of length n^3. The average image vector is computed as $\mu = \frac{1}{M}\sum_{i=1}^{M} X^{(i)}$. The average microstructure (μ) is then subtracted from all the image vectors as $X^{(i)} \leftarrow X^{(i)} - \mu$ for $i = 1, \ldots, M$. The eigenvectors $U^{(k)}$ of the $n^3 \times n^3$ covariance matrix $C = \frac{1}{M}\sum_{i=1}^{M} X^{(i)} X^{(i)}$ satisfying the equation

$$CU^{(k)} = \lambda_k U^{(k)}, \quad k = 1, \ldots, n^3, \tag{7}$$

along with the eigenvalues λ_k are computed. This set of eigen-images and eigenvalues form the best basis to represent the microstructures. The computation of these n^3 basis becomes a computationally intensive process because of the very large dimensionality (n^3) of the correlation matrix. The 'method of snapshots' provides a computationally more efficient way to compute these basis images (refer [49] for a discussion of the method of snapshots and see [50] for details on efficiently computing the basis images).

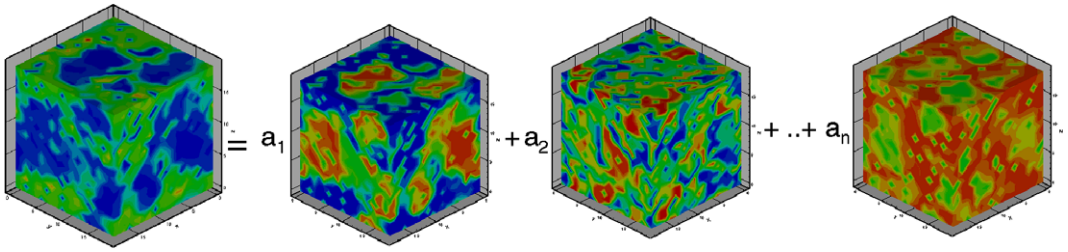

Fig. 2. Any microstructure is represented as a linear combination of the eigen-images.

The first N eigen-images (usually $N \ll M$) representing most of the energy spectrum of the decomposition is chosen. Any random microstructure (I) belonging to the space of allowable microstructures Ω can then be represented as a unique linear combination of the N eigen-images (see Fig. 2):

$$I = \mu + \sum_{i=1}^{N} a_i U^{(i)}, \quad I \in \Omega, (a_1, \ldots, a_N) \in \mathbb{R}^N. \tag{8}$$

Let us denote the transformation of any microstructure (its digitized image) $I \in \Omega$ into the set of N real coefficients $a_1, \ldots, a_N$ by $\mathscr{F}$. The function $\mathscr{F} : \Omega \to \mathbb{R}^N$ represents the reduced-order model of the infinite-dimensional space Ω in N dimensional space.

Remark 5. It is important to note that $\mathscr{F}$ is injective but *not* surjective. That is, every microstructure $I_k \in \Omega$ has a unique mapping $(a_1^{(k)}, \ldots, a_N^{(k)}) \in \mathbb{R}^N$. On the other hand, every point $(a_1^{(m)}, \ldots, a_N^{(m)}) \in \mathbb{R}^N$ results in a microstructure I_m that need not belong to Ω.

For the mapping to be useful in the solution of the stochastic partial differential equation Eq. (2) describing diffusion through random heterogeneous media, $\mathscr{F}$ has to be made bijective. The co-domain of $\mathscr{F}$ has to be contracted to $\mathscr{H} \subset \mathbb{R}^N$ such that $\mathscr{F} : \Omega \to \mathscr{H}$ is bijective. That is, we have to construct the space of allowable N-tuples $(a_1^{(m)}, \ldots, a_N^{(m)}) \in \mathscr{H} \subset \mathbb{R}^N$ whose images I_m belong to Ω. This is shown schematically in Fig. 3.

4.1. Constructing the subspace $\mathscr{H}$

An alternate, equivalent definition of the space $\mathscr{H} \subset \mathbb{R}^N$, that will clarify the contraction procedure, is given as

Find the largest proper subset $\mathscr{H} \subset \mathbb{R}^N$ such that, for any point $(a_1, \ldots, a_N) \in \mathscr{H}$, the image $I = \mu + \sum_{i=1}^{N} a_i U^{(i)}$ belongs to the space Ω.

Every image $I \in \Omega$ satisfies certain statistical properties $P_1, \ldots, P_m$. These statistical properties can now be used to provide bounds on the values that the N-tuple $(a_1, \ldots, a_N)$ can take. We systematically develop these constraints below.

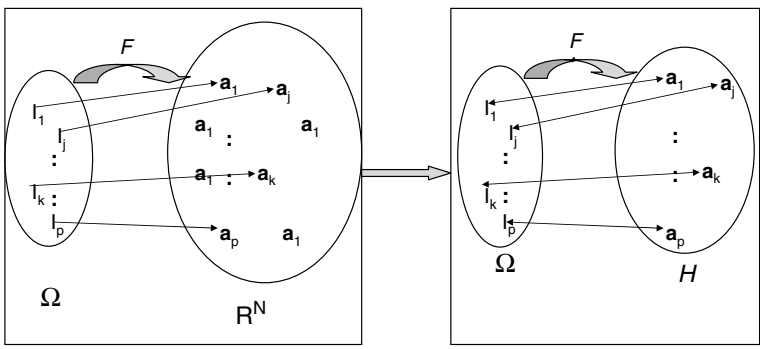

Fig. 3. To make the mapping $\mathscr{F}$ bijective, its range has to be contracted from $\mathbb{R}^N$ to $\mathscr{H}$.

4.1.1. Bounds on the pixel values

Each pixel in the image can only take values in a bounded interval, usually $[0,1]$. Denote the range of possible values by $[p_l, p_h]$. The bounds on the N-tuple can be written as

$$p_l \leqslant \mu(\beta) + \sum_{i=1}^{N} a_i U^{(i)}(\beta) \leqslant p_h, \quad \beta = 1, \ldots, n^3, \tag{9}$$

where β ranges over all the n^3 pixels in the image. This results in a set of $2n^3$ linear (inequality) constraints on the N-tuple.

4.1.2. Constraints through first-order statistics: volume fraction

The volume fraction of the phase 1 of any reconstructed microstructure must be equal to ϕ_1. This results in a linear equality constraint on the N-tuple given by

$$\phi_1 = \langle I \rangle = \left\langle \mu + \sum_{i=1}^{N} a_i U^{(i)} \right\rangle = \langle \mu \rangle + \left\langle \sum_{i=1}^{N} a_i U^{(i)} \right\rangle = \langle \mu \rangle + \sum_{i=1}^{N} a_i \langle U^{(i)} \rangle,$$

from which we can write the following:

$$\phi_1 = b_0 + \sum_{i=1}^{N} a_i b_i, \tag{10}$$

where $b_i = \langle U^{(i)} \rangle$ is the mean value of the individual eigen-images and b_0 is the mean value of the mean image. For ease of notation, we set $U^0 = \mu$ and $a_0 = 1$.

4.1.3. Constraints through second-order statistics: 2-point correlation

Enforcing the condition that the 2-point correlation of the reconstructed image must satisfy the given function $S(r)$ results in a set of quadratic equality constraints. This can be derived as follows:

$$\begin{aligned} S_2(r) = \langle I(\boldsymbol{x}) I(\boldsymbol{x}+\boldsymbol{r}) \rangle &= \left\langle \left[\sum_{i=0}^{N} a_i U^{(i)}(\boldsymbol{x}) \right] \left[\sum_{j=0}^{N} a_j U^{(j)}(\boldsymbol{x}+\boldsymbol{r}) \right] \right\rangle = \left\langle \sum_{i=0}^{N} \sum_{j=0}^{N} [a_i U^{(i)}(\boldsymbol{x})][a_j U^{(j)}(\boldsymbol{x}+\boldsymbol{r})] \right\rangle \\ &= \sum_{i=0}^{N} \sum_{j=0}^{N} a_i a_j \langle U^{(i)}(\boldsymbol{x}) U^{(j)}(\boldsymbol{x}+\boldsymbol{r}) \rangle, = \sum_{i=0}^{N} \sum_{j=0}^{N} a_i a_j \frac{1}{\Theta} \int_{\Theta} \frac{1}{V} \int_{V} U^{(i)}(\boldsymbol{x}) U^{(j)}(\boldsymbol{x}+r\boldsymbol{e}_v) \, \mathrm{d}\boldsymbol{x} \, \mathrm{d}v, \end{aligned}$$

from which we can write the following:

$$S_2(r) = \sum_{i=0}^{N} \sum_{j=0}^{N} a_i a_j C_{ij}(r), \tag{11}$$

where $C_{ij}(r) = \frac{1}{\Theta} \int_{\Theta} \frac{1}{V} \int_{V} U^{(i)}(\boldsymbol{x}) U^{(j)}(\boldsymbol{x}+r\boldsymbol{e}_v) \, \mathrm{d}\boldsymbol{x} \, \mathrm{d}v$.

The total number of these constraints is equal to the range of r in the equation above. Usually, for discretized images, r takes a small number of integer values $r = 1, \ldots, q$. Enforcing the two-point correlation function results in a set of q quadratic equality constraints.

4.1.4. Computational complexity of enforcing constraints

The subspace $\mathscr{H}$ is constructed by solving a constrained minimization problem with the given constraints. It is relatively simple to solve for $\mathscr{H}$ when only the pixel constraints Eq. (9) and the first-order statistic of volume fraction Eq. (10) are enforced. These result in a set of linear inequalities and one linear equality constraint. This is a simple problem in linear programming, where the subspace is a convex hull [51]. Let $\boldsymbol{a} = (a_1, \ldots, a_N)$ denote any point in $\mathscr{H}$:

Find the region $\mathscr{H} \subset \mathbb{R}^N$ that satisfies $\sum_{i=0}^{N} a_i b_i = \phi_1$,
subject to the constraints $p_l \leqslant \sum_{i=0}^{N} a_i U^{(i)}(\beta) \leqslant p_h, \quad \beta = 1, \ldots, n^3.$

Enforcing second-order statistics (along with the first-order statistic and the pixel constraints) becomes a problem in quadratic programming [51].

$$\begin{aligned}&\text{Find the region } \mathscr{H} \subset \mathbb{R}^N \text{ that minimizes } \mathscr{G}(\boldsymbol{a}) = |\boldsymbol{a}'\mathbf{C}(r)\boldsymbol{a} - S(r)|\\ &\quad \text{subject to the constraints } \sum_{i=0}^{N} a_i b_i = \phi_1, \text{ and}\\ &\quad p_l \leqslant \sum_{i=0}^{N} a_i U^{(i)}(\beta) \leqslant p_h, \quad \beta = 1, \ldots, n^3,\end{aligned}$$

where $\mathbf{C}(r)$ is the matrix notation of $C_{ij}(r)$. There are various procedures, like the active set method and the preconditioned conjugate gradient method that can be used to find the subspace $\mathscr{H}$ [51].

Remark 6. Once $\mathbf{C}(r)$ has been computed, evaluation of the quadratic function $\mathscr{G}(\boldsymbol{a})$ is just a set of matrix-vector multiplies.

Higher-order statistics can be similarly enforced. A systematic way to find the subspace $\mathscr{H}$ is to sequentially apply the constraints of the statistical properties, starting form the first-order constraints. This is schematically shown next.

4.1.5. Sequential contraction of the subspace: a numerical illustration

In this sub-section, we illustrate the methodology formulated above to find the subspace $\mathscr{H}$. For the sake of simplicity and ease of visualization, we assume that the number of eigen-images is considered to be 3. $\mathscr{H}$ is a subspace of $\mathbb{R}^3$.

First $\mathscr{H}$ is set equal to $\mathbb{R}^3$. The equality constraint of the volume fraction is applied next. This can be used to represent one of the variables (say a_3) in terms of the other two variables (a_1,a_2). This constraint ensures that the allowable set of points lie on the plane defined by $a_3 = \frac{\phi - a_1 b_1 - a_2 b_2}{b_3}$. This plane is visualized in Fig. 4a. Next, the pixel bounds on the mapped image are enforced. This is a set of convex linear inequality constraints. This convex set of constraint inequalities is converted into the set of vertices at the intersections of those inequalities. This is called the 'vertex enumeration' problem in linear programming. A primal-dual polytope method is employed in MatLab to construct the set of vertices [52]. The resulting convex hull is visualized in Fig. 4b. A second-order statistic in the form of the two-point correlation is chosen. For simplicity, we only enforce the value of $L(2)$. This constraint results in a quadratic programming problem. The resulting surface is plotted in Fig. 4c. This surface is the contracted subspace $\mathscr{H}$.

4.2. The low-dimensional model $\mathscr{G} : \mathscr{H} \rightarrow \Omega$: the 'material' plane

$\mathscr{H}$ represents the space of coefficients $(a_1, \ldots, a_N)$ that map to microstructures that satisfy the statistical properties $P_1, \ldots, P_n$. The first-order constraints ensures that $\mathscr{H}$ is a truncated plane in N-dimensional space. Since every point on this plane represents a unique microstructure, we call this plane the 'material' plane.

Since each of the microstructures in the 'material' plane satisfies all required statistical properties, they are equally probable to occur in any random spatial point in the large scale structure. That is, every point in the

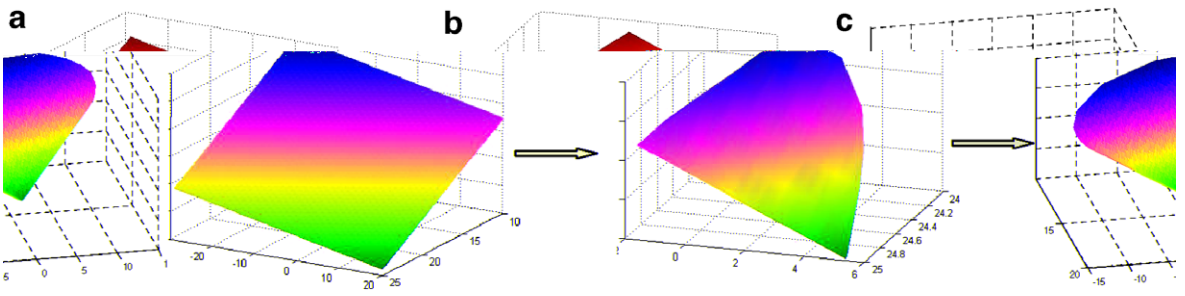

Fig. 4. Sequential contraction of $\mathbb{R}^3$ to $\mathscr{H}$: (a) Enforcing the first-order statistics. (b) Enforcing the pixel bounds; and (c) : Enforcing one second-order statistic.

'material' plane is equiprobable. This observation provides a way to construct the stochastic model for the allowable microstructures:

Define the function $\mathscr{G} : \mathscr{H} \to \Omega$ such that $I(\omega) = \mu + \sum_{i=1}^{N} \xi_i U^{(i)}$, $i = 1, \ldots, N$, where ξ_i are independent uniform random variables chosen from $\mathscr{H}$. By the subspace contraction procedure developed above, $\mathscr{F} : \Omega \to \mathscr{H}$ was made bijective. $\mathscr{G}$ is just the inverse of $\mathscr{F}$. This low-dimensional stochastic model $\mathscr{G}$ for the microstructure is the stochastic input in the partial differential equation defining the problem. Techniques to solve the problem are discussed in the next two sections.

Remark 7. We wish to emphasize the fact that the methodology outlined above is very general. Any other technique for model reduction (instead of using principle component analysis) can also be used to obtain a reduced image set. Other applicable techniques include independent component analysis, other transform techniques like the cosine transform, the Haar transform as well as filtering techniques like Autoregressive (AR), Moving-average (MA) and Auto Regressive Moving Average (ARMA) methods. Once the dataset has been approximated as coefficients in N-dimensional space, the bounds on these coefficients can be computed using the techniques outlined in this section.

5. Collocation techniques for solving stochastic partial differential equations

Recall that the governing equation for thermal diffusion is given by Eq. (2) From the developments of the previous section, $\alpha(\omega)$ can now be represented as a function, F, which depends on the topology as:

$$\alpha(\omega) = \alpha(\xi_1, \ldots, \xi_N) = F\left(\mu + \sum_{i=1}^{N} \xi_i U^{(i)}\right), \quad i = 1, \ldots, N. \tag{12}$$

The reduced $N + d$-dimensional equation for the temperature with N stochastic dimensions and d spatial dimensions is given by Eq. (4) where Γ, the domain of the N-tuple $\boldsymbol{\xi} = (\xi_1, \ldots, \xi_N)$ is the subspace $\mathscr{H}$.

Usually, for realistic problems, the number of stochastic dimensions is usually large ($N > 8$). As discussed in Section 1, it is difficult to use the spectral Galerkin method in these cases, because of the coupled nature of the resulting deterministic equations. We utilize an alternate collocation based strategy that results in a set of decoupled deterministic equations [17]. In the collocation approach, a finite element approximation is used for the spatial domain and while the multi-dimensional stochastic space is approximated using interpolating functions. The interpolating functions are mutually orthogonal and the resulting equations are decoupled. In this method, one computes the deterministic solution at various points in the stochastic space and then builds an interpolated function that best approximates the required solution [17–19,22,23].

The collocation method collapses the $N + d$-dimensional problem to solving M (where, M is the number of collocation points) deterministic problems in d dimensions. The statistics of the random solution can be obtained through simple quadrature operations on the interpolation function $u = \sum_{k=1}^{M} u(x, \boldsymbol{\xi}_k) L_k(\boldsymbol{\xi})$

$$\langle u^{\alpha}(x) \rangle = \sum_{k=1}^{M} u^{\alpha}(x, \boldsymbol{\xi}_k) \int_{\Gamma} L_k(\boldsymbol{\xi}) \rho(\boldsymbol{\xi}) \, \mathrm{d}\boldsymbol{\xi}, \tag{13}$$

where $\rho(\boldsymbol{\xi}) : \Gamma \to \mathbb{R}$ is the joint probability distribution function for the set of independent, uniformly distributed random variables $\xi_1, \ldots, \xi_N$.

There are two issues to be considered while constructing the interpolating function: Which set of nodes $\Theta_N = \{\boldsymbol{\xi}_i^n\}_{i=1}^{M}$ is optimal, and once the set of points are decided how does one construct the multi-dimensional interpolation function.

The choice of the optimal distribution of points is motivated using one-dimensional functions. Let $f : [a, b] \to \mathbb{R}$ be a function that has to be interpolated by a polynomial $\mathscr{I}_m(f)$ using a finite number of nodes $a \leqslant x_0 < x_1 \ldots < x_m \leqslant b$. There exists a (unique) polynomial $\mathscr{I}_m(f)$ satisfying $\mathscr{I}_m(f)(x_i) = f(x_i)$ for $i = 0, 1 \ldots, m$. This can be written in the form: $\mathscr{I}_m(f)(x) = \sum_{i=0}^{m} f(x_i) L_i(x)$, where the basis polynomials are given by $L_i(x) = \prod_{k=0, k \neq i}^{m} \frac{x - x_k}{x_i - x_k}$. As the number of points m increases, the interpolation function $\mathscr{I}_m(f)$ represents the function f better. This is irrespective of how one chooses the nodes $\{x_i\}_{i=0}^{m}$. However, uniform

convergence ($\|f - \mathscr{I}_m(f)\|_\infty \to 0$ as $m \to \infty$) is guaranteed only for a particular distribution of points. This optimal node distribution is derived form the theory of *the best approximating polynomial* and its Lebesgue constant [26]. One such type of node distribution is the interpolation based at the Chebyshev extrema [25]. The error bound for the Chebyshev node based interpolation function of the function $f \in \mathscr{C}^k$ is given by [26]

$$\|f - \mathscr{I}^X(f)\|_\infty \leqslant Cn^{-k}\log(n). \tag{14}$$

When one is dealing with multiple stochastic dimensions, it is straightforward to extend the interpolation functions developed in one dimension to multiple dimensions as simple tensor products. If $u(\boldsymbol{\xi})$ is a function that has to be approximated in N dimensional space, and $\mathbf{i} = (m_1, m_2, \ldots m_N)$ are the number of nodes used in the interpolation in N dimensions, the full-tensor product interpolation formula is given as

$$\mathscr{I}^N u(\boldsymbol{\xi}) = (\mathscr{I}^{i_1} \otimes \ldots \otimes \mathscr{I}^{i_N})(u)(\boldsymbol{\xi}) = \sum_{j_1=1}^{m_1} \ldots \sum_{j_N=1}^{m_N} u(\xi_{j_1}^{i_1}, \ldots, \xi_{j_N}^{i_N}).(L_{j_1}^{i_1} \otimes \ldots \otimes L_{j_N}^{i_N}), \tag{15}$$

where $\mathscr{I}^{i_k}$ are the interpolation functions in the i_k direction and $\xi_{j_m}^{i_k}$ is the mth point in the kth coordinate. Clearly, the above formula needs $m_1 \times \ldots \times m_N$ function evaluations, at points sampled on a regular grid. In the simplest case of using only two points in each dimension, the total number of points required for a full-tensor product interpolation is $M = 2^N$. This number grows very quickly as the number of dimensions is increased. Thus one has to look at intelligent ways of sampling points in the regular grid described by the full-tensor product formula so as to reduce the number of function evaluations required.

The Smolyak algorithm provides a way to construct interpolation functions based on a minimal number of points in multi-dimensional space. Using Smolyak's method, univariate interpolation formulae are extended to the multivariate case by using tensor products in a special way. This provides an interpolation strategy with potentially orders of magnitude reduction in the number of support nodes required. The algorithm provides a linear combination of tensor products chosen in such a way that the interpolation property is conserved for higher dimensions.

5.1. Smolyak's construction of sparse sets

Consider the one-dimensional interpolation formula

$$\mathscr{U}^m(f) = \sum_{j=1}^{m} f(Y_k^j) a_k^j, \tag{16}$$

where Y_k^i are the nodal sets and $a_k^i \in C[a,b]$ are the interpolating functions. The Smolyak algorithm constructs the sparse interpolant as [25,26]

$$A_{q,N}(f) = \sum_{q-N+1 \leqslant |\mathbf{i}| \leqslant q} (-1)^{q-|\mathbf{i}|}.\binom{N-1}{q--\mathbf{i}}.(\mathscr{U}^{i_1} \otimes \ldots \otimes \mathscr{U}^{i_N}), \tag{17}$$

with $A_{N-1,N} = 0$ and where $\mathbf{i} = (i_1, \ldots, i_N) \in \mathbb{N}^N$ and $|\mathbf{i}| = i_1 + \ldots + i_N$. The structure of the points becomes clearer when one considers the incremental interpolant, Δ^i given by [25,26]

$$\mathscr{U}^0 = 0, \quad \Delta^i = \mathscr{U}^i - \mathscr{U}^{i-1}. \tag{18}$$

The Smolyak interpolation $\mathscr{A}_{q,d}$ (the level q interpolant in d dimensions) is then given by

$$\mathscr{A}_{q,d}(f) = \sum_{|\mathbf{i}| \leqslant q} (\Delta^{i_1} \otimes \ldots \otimes \Delta^{i_d})(f) = \mathscr{A}_{q-1,d}(f) + \sum_{|\mathbf{i}|=q} (\Delta^{i_1} \otimes \ldots \otimes \Delta^{i_d})(f). \tag{19}$$

To compute the interpolant $\mathscr{A}_{q,d}(f)$ from scratch, one needs to compute the function at the nodes covered by the sparse grid $\mathscr{H}_{q,N}$

$$\mathscr{H}_{q,N} = \bigcup_{q-N+1 \leqslant |\mathbf{i}| \leqslant q} (\Theta_1^{i_1} \times \ldots \times \Theta_1^{i_N}). \tag{20}$$

But the construction of the algorithm allows one to utilize all the previous results generated to improve the interpolation. Choosing the Chebyshev points as the support nodes in the one-dimensional case ensures that

the sets of points Θ^i are nested ($\Theta^i \subset \Theta^{i+1}$). To extend the interpolation from level i to $i+1$, one has to evaluate the function at the grid points $\Theta^i_\Delta = \Theta^i \setminus \Theta^{i-1}$. Thus, to go from an order $q-1$ interpolation to an order q interpolation, one only needs to evaluate the function at the differential nodes $\Delta\mathscr{H}_{q,N}$ given by

$$\Delta\mathscr{H}_{q,N} = \bigcup_{|\mathbf{i}|=q} (\Theta^{i_1}_\Delta \otimes \ldots \otimes \Theta^{i_N}_\Delta). \tag{21}$$

As a matter of notation, the interpolation function used will be denoted $A_{N+k,N}$, where k is called the level of the Smolyak construction. The interpolation error using the piecewise multilinear basis is [25,26]

$$\|f - A_{q,N}(f)\| = \mathscr{O}(M^{-2}|\log_2 M|^{3(N-1)}), \tag{22}$$

where $M = \dim(\mathscr{H}(q,N))$ is the number of interpolation points.

5.2. Solution strategy

The final solution strategy is as follows: A stochastic collocation method in $\mathscr{H} \equiv \Gamma \subset \mathbb{R}^N$ along with a finite element discretization in the physical space $D \subset \mathbb{R}^d$ is used. Given a particular level of interpolation of the Smolyak algorithm in N-dimensional random space, we define the set of collocation nodes $\Theta_N = \{\boldsymbol{\xi}_k\}_{k=1}^M$ on which the interpolation function is constructed. Given a piecewise FEM mesh $X^h_d \in H^1_0(D)$, find, for $k = 1, \ldots, M$,

$$u^h_k(x) = u^h(x, \boldsymbol{\xi}_k) \in X^h_d, \tag{23}$$

such that

$$\mathscr{B}(u(\boldsymbol{\xi}_i) : \boldsymbol{\xi}_i, x, t) = 0, \quad i = 1, \ldots, M. \tag{24}$$

The final numerical solution takes the form

$$u_h(x, \boldsymbol{\xi}) = \sum_{k=1}^{M} u^h_k(x) L$$

$$u(x,t) = u_d(x), \quad x \in \partial D_D, \tag{28}$$

$$u(x,0) = 0, \quad x \in D. \tag{29}$$

Define the function space V_0 such that

$$V_0 = L_2(\mathscr{T}) \times H^1(D) \equiv \left\{ v : \int_{\mathscr{T}} \int_D (v^2(x,t) + (\nabla v(x,t))^2)\, \mathrm{d}x\, \mathrm{d}t < \infty \right\}. \tag{30}$$

The function space for the solution U and the trial function space V is defined as

$$U = \{u : u \in V_0, u = u_d, x \in \partial D_D\}, \quad V = \{v : v \in V_0, v = 0, x \in \partial D_D\}. \tag{31}$$

The variational form of Eq. (27) can be written as: find $u \in U$ such that for all $v \in V$

$$(u_{,t}, v) + (\alpha \nabla u, \nabla v) = (f, v), \tag{32}$$

where $(u, v) \equiv \int_D uv\, \mathrm{d}x$. We closely follow our earlier work [27] in deriving the variational multiscale formulation.

In the variational multiscale approach, the exact solution u is assumed to be made up of contributions from two different scales namely, the coarse scale solution u^C that can be resolved using a coarse mesh and a subgrid solution $u^F (u = u^C + u^F)$. This additive sum decomposition induces a similar decomposition for the function spaces as $U = U^C \oplus U^F$ and $V = V^C \oplus V^F$, respectively. The main idea is to develop models for characterizing the effect of the subgrid solution u^F on the coarse scale solution and to subsequently derive a modified coarse scale formulation that only involves u^C. The variational formulation given in Eq. (32) is split into two equations representing each of the scales:

$$(u^C_{,t} + u^F_{,t}, v^C) + (\alpha \nabla u^C + \alpha \nabla u^F, \nabla v^C) = (f, v^C), \quad \forall v^C \in V^C, \tag{33}$$

$$(u^C_{,t} + u^F_{,t}, v^F) + (\alpha \nabla u^C + \alpha \nabla u^F, \nabla v^F) = (f, v^F), \quad \forall v^F \in V^F. \tag{34}$$

Eq. (34) can be solved (usually by making some locality assumptions) to obtain an approximate model for the subgrid solution u^F. This model can then be used in Eq. (33) to eliminate u^F and obtain a modified formulation only in terms of u^C.

Assume that the spatial domain is discretized using a coarse mesh into Nel disjoint sub-domains (also referred to as coarse elements) denoted as $D^{(e)}$, where, (e) denotes the coarse element number. Further, let each coarse element be discretized using a subgrid mesh into $\mathrm{Nel}^F_{(e)}$ disjoint sub-domains (also referred to as subgrid elements). The subgrid solution is assumed to be made up of two components $\hat{u}^F$ and u^{F0} such that

$$(u^C{}_{,t}, v^F) + (\hat{u}^F{}_{,t}, v^F) + (\alpha \nabla u^C, \nabla v^F) + (\alpha \nabla \hat{u}^F, \nabla v^F) = 0, \tag{35}$$

$$(u^{F0}{}_{,t}, v^F) + (\alpha \nabla u^{F0}, \nabla v^F) = (f, v^F). \tag{36}$$

The solution component $\hat{u}^F$ incorporates the entire coarse scale solution information and u^{F0} has no dependence on the coarse scale solution. Further, the dynamics of u^{F0} is driven by the projection of the source term onto the subgrid scale function space. This can be also understood as the sum of the homogeneous solution with a particular solution. Following our earlier work [27], we refer to $\hat{u}^F$ as the coarse-to-subgrid ($C2S$) map [27]. Owing to the affine nature of Eq. (36), u^{F0} is called the affine correction term [27]. This decomposition of u^F into $\hat{u}^F$ and u^{F0} has its roots in Green's function theory and has been utilized in deriving VMS based mixed variational formulations for deterministic elliptic [2] equations. Until now, Eqs. (35) and (36) are defined over the entire domain and are exact. In order to localize the calculations of the subgrid solution, Eqs. (35) and (36) can be localized to a coarse element $D^{(e)}$ with the only difference that the C2S map $\hat{u}^F$, the affine correction u^{F0} and the trial function v^F belong to a restriction (denoted as $V_0^{(e)}$) of the function space V_0 to the coarse element with suitable boundary conditions (for example, the trial functions need to be zero on the coarse element boundaries, whereas, the C2S map can be non-zero). The derivations below are performed for a single coarse element $D^{(e)}$.

6.1. C2S map and multiscale basis functions

Let us assume that in a fully-resolved direct numerical simulation, the dynamics of the exact solution can be captured using a fine time-step of δt. Since the length scales of interest in the coarse solution are far greater

than that of the exact solution, we assume that the coarse time-step Δt is much larger in comparison to δt. Let us consider a coarse time-step $\Delta t = [t_n, t_{n+1}]$. Let t' be the local time coordinate defined such that at t_n, $t' = 0$ and at t_{n+1}, $t' = \Delta t$.

Let us also assume a piecewise polynomial finite element representation for the coarse solution inside a coarse element $D^{(e)}$ ((e) is suppressed herein to simplify notation):

$$u^C(x,t) = \sum_{\beta=1}^{\mathrm{Nbf}} u^C_\beta(t')\Psi_\beta(x), \tag{37}$$

where Nbf denotes the number of finite-element shape functions (piecewise polynomials) defined on the coarse element. We seek a similar representation for the C2S map of the following functional form:

$$\hat{u}^F(x,t) = \sum_{\beta=1}^{\mathrm{Nbf}} u^C_\beta(t')\phi^F_\beta(x,t'). \tag{38}$$

The fine scale variational formulation of Eq. (35) can be re-written after substitution of Eqs. (37) and (38) as follows:

$$(u^C_{\beta,t}\Psi_\beta, v^F) + (u^C_{\beta,t}\phi^F_\beta + u^C_\beta\phi^F_{\beta,t}, v^F) + (\alpha u^C_\beta\nabla\phi^F_\beta, \nabla v^F) + (\alpha u^C_\beta\nabla\Psi_\beta, \nabla v^F) = 0, \tag{39}$$

where the repeated indices β indicates a summation over $1,\ldots,\mathrm{Nbf}$ (with similar notation applied to subsequent equations as well). The above equation can be further simplified as follows:

$$\left(\left\{u^C_\beta(\Psi_\beta + \phi^F_\beta)\right\}_{,t}, v^F\right) + \left(\alpha\nabla\left\{u^C_\beta(\Psi_\beta + \phi^F_\beta)\right\}, \quad \nabla v^F\right) = 0. \tag{40}$$

Without loss of generality, we can assume the following representation for the coarse scale nodal solutions $u^C_{\beta s}(t)$ inside the coarse time-step

$$u^C_\beta(t') = A(t')\tilde{u}^C_\beta + B(t')\bar{u}^C_\beta, \tag{41}$$

where $\tilde{u}^C_{\beta s}$ and $\bar{u}^C_{\beta s}$ denote the nodal values of the coarse solution at the start and end of the coarse time step, respectively. $A(t')$ and $B(t')$ are special positive functions that obey the following relations:

$$A(t') + B(t') = 1, \quad A(0) = 1, \quad A(\Delta t) = 0, \quad B(0) = 0, \quad \text{and} \quad B(\Delta t) = 1. \tag{42}$$

The representation given in Eq. (41) is quite general and incorporates several well-known time integration rules. For example, $A(t') = (\Delta t - t')/\Delta t$ and $B(t') = t'/\Delta t$ yields a backward-Euler time integration rule. From Eqs. (38) and (41), we can write the C2S map as follows:

$$\hat{u}^F_\beta(x,t) = \sum_{\beta=1}^{\mathrm{Nbf}} \left[\tilde{u}^C_\beta A(t')\phi^F_\beta(x,t') + \bar{u}^C_\beta B(t')\phi^F_\beta(x,t')\right]. \tag{43}$$

We can now write Eq. (40) as

$$\begin{aligned}\tilde{u}^C_\beta\left\{\left(\left\{A(t')(\Psi_\beta + \phi^F_\beta)\right\}_{,t}, v^F\right) + \left(\alpha\nabla\left\{A(t')(\Psi_\beta + \phi^F_\beta)\right\}, \nabla v^F\right)\right\} \\ + \bar{u}^C_\beta\left\{\left(\left\{B(t')(\Psi_\beta + \phi^F_\beta)\right\}_{,t}, v^F\right) + \left(\alpha\nabla\left\{B(t')(\Psi_\beta + \phi^F_\beta)\right\}, \nabla v^F\right)\right\} = 0.\end{aligned} \tag{44}$$

Note that the above equation is fully-characterized based on the values taken by $\tilde{u}^C_{\beta s}$ and $\bar{u}^C_{\beta s}$ and the subgrid basis function $\phi^F_{\beta s}$.

We are looking to construct a localized scheme for representation of the subgrid solutions. Further, this localized scheme should hold for all possible values of the coarse nodal coefficients $\tilde{u}^C_\beta$ and $\bar{u}^C_\beta$. Hence, we equate the terms in parentheses to zero to obtain the following set of variational formulations defined for each index β, where, $\beta = 1,\ldots,\mathrm{Nbf}$.

$$\left(\left\{A(t')(\Psi_\beta + \phi^F_\beta)\right\}_{,t}, v^F\right) + \left(\alpha\nabla\left\{A(t')(\Psi_\beta + \phi^F_\beta)\right\}, \nabla v^F\right) = 0, \tag{45}$$

$$\left(\left\{B(t')(\Psi_\beta+\phi^F_\beta)\right\}_{,t},v^F\right)+\left(\alpha\nabla\left\{B(t')(\Psi_\beta+\phi^F_\beta)\right\},\nabla v^F\right)=0. \tag{46}$$

Now, by using the relations $A(t')+B(t')=1$, we can simplify Eq. (46) as follows:

$$\left((\Psi_\beta+\phi^F_\beta)_{,t},v^F\right)+\left(\alpha\nabla(\Psi_\beta+\phi^F_\beta),\nabla v^F\right)-\left(\left\{A(t')(\Psi_\beta+\phi^F_\beta)\right\}_{,t},v^F\right)-\left(\alpha\nabla\left\{A(t')(\Psi_\beta+\phi^F_\beta)\right\},\nabla v^F\right)=0. \tag{47}$$

By combining Eqs. (47) and (45), we obtain the evolution equation for ϕ^F_β

$$\left((\Psi_\beta+\phi^F_\beta)_{,t},v^F\right)+\left(\alpha\nabla(\Psi_\beta+\phi^F_\beta),\nabla v^F\right)=0. \tag{48}$$

By assuming twice-differentiability of the subgrid basis functions, we can write the strong formulation for Eq. (48) as: Find ϕ^F_β for $\boldsymbol{x}\in D^{(e)}$ and $t\in[t_n,t_{n+1}]$ such that

$$\phi^F_{\beta,t}-\nabla\cdot\left(\alpha(x)\nabla\phi^F_\beta\right)-\nabla\cdot\left(\alpha(x)\nabla\Psi_\beta(x)\right)=0. \tag{49}$$

Solving the above equation for ϕ^F_β involves additional computation of the term $\alpha(\boldsymbol{x})\nabla\Psi_\beta(\boldsymbol{x})$. To avoid that, we introduce a new variable Φ_β

$$\Phi_\beta(x,t')=\Psi_\beta(x)+\phi^F_\beta(x,t'), \tag{50}$$

that simplifies Eq. (49) to the following equation

$$\Phi_{\beta,t}-\nabla\cdot(\alpha(x)\nabla\Phi_\beta)=0. \tag{51}$$

In order to complete the specification of this equation, we need to provide boundary conditions for Φ_β on the coarse-element boundaries $\partial D^{(e)}$. We use ideas from the multiscale finite element method [6] that indicate that the behavior of Φ_β on the boundaries of the coarse element should retain the characteristics of Eq. (51). Dirichlet boundary conditions are applied on the boundaries of the coarse element. These boundary conditions are obtained in a sequential manner: First, a one dimensional problems of the same form as Eq. (51) is solved. The boundary conditions are set to the nodal values of the corresponding coarse scale basis functions. This one dimensional equation is solved on all the edges of the coarse element. These solutions are then used as boundary conditions for solving the two dimensional equation (of the same form as Eq. (51)) on all the element faces. The solutions on the faces of the coarse element are subsequently used as the Dirichlet boundary conditions for the solution of Φ_β (refer [6,27]).

The affine correction term u^{F0} as defined by Eq. (36) leads to the following strong form of equations inside each coarse element sub-domain

$$u^{F0}{}_{,t}+\nabla\cdot(\alpha\nabla u^{F0})=f,\ x\in D^{(e)}. \tag{52}$$

We can now substitute Φ_β and u^{F0} in the coarse scale variational formulation given in Eq. (53) to obtain the following: In each coarse element $D^{(e)}$,

$$(u^C_{\beta,t}\Phi_\beta,v^C)+(u^C_\beta\Phi_{\beta,t},v^C)+(u^C_\beta\alpha\nabla\Phi_\beta,\nabla v^C)=(f,v^C)-(\alpha\nabla u^{F0},\nabla v^C)-(u^{F0}{}_{,t},v^C). \tag{53}$$

Thus, the affine correction term figures in the modified coarse scale variational formulation as a sum of two terms: an anti-diffusive term and a term involving its time derivative. Eq. (53) can be written as a matrix-vector equation on each coarse element $D^{(e)}$

$$[M(t)]\{u^C{}_{,t}\}+[K(t)]\{u^C\}=\{f(t)\}, \tag{54}$$

where, the dependence of $[M(t)]$, $[K(t)]$ and $\{f(t)\}$ on time comes from the basis functions Φ_β and the time varying source term $f(\boldsymbol{x},t)$, respectively as follows:

$$\begin{aligned}
[M]&=\left(\Phi_\beta(x,t'),\Psi_\alpha(x)\right),\\
[K]&=\left(\alpha(x)\nabla\Phi_\beta(x,t'),\nabla\Psi_\alpha(x)\right)+\left(\Phi_{\beta,t}(x,t'),\Psi_\alpha(x)\right),\\
\{f\}&=(f(x,t),\Psi_\alpha(x))-\left(\{u^{F0}(x,t')\}_{,t},\Psi_\alpha(x)\right)-\left(\alpha(x)\nabla u^{F0}(x,t'),\nabla\Psi_\alpha(x)\right),
\end{aligned} \tag{55}$$

and $\{u^C\}$ represent the nodal values of the coarse solution in each coarse element. The deterministic VMS problem in efficiently solved in a parallel C++ framework. Each processor computes the fine-scale basis functions for a set of coarse elements and constructs a part of the global stiffness matrix and load vector.

Remark 8. In most practical problems of interest, the assumption of a quasi-static subgrid solution is made i.e. in the governing equations for subgrid basis functions Φ_β, we assume that $\Phi_{\beta,t} = 0$. This reduces the computational cost since the subgrid basis functions can be computed once and for all at the start of the computation (refer [27] for a detailed discussion). This approach is followed in the validation and all other examples reported in the rest of the paper.

6.1.1. Reconstruction of the fine scale solution

Given the coarse scale solution $\{u^C\}$, the subgrid basis functions ϕ_β and the affine correction u^{F0}, the reconstructed fine scale VMS solution is given by

$$u = \sum_{\beta=1}^{\mathrm{Nbf}} u^C_\beta \Phi_\beta + u^{F0}(x). \tag{56}$$

6.1.2. Validation of the VMS code

In our previous work [27], Velamur Asokan and Zabaras had developed a stochastic variational multiscale framework utilizing the generalized polynomial chaos expansion method. In the present work, we utilize a deterministic variant of the method. For the sake of completeness, we include a comparison of the VMS framework with fully-resolved FEM calculations. A two-phase microstructure containing $65 \times 65 \times 65$ pixels is considered (Fig. 5). The microstructure is a tungsten–silver composite (see Section 7). The volume fraction of silver in this composite is 20%. The thermal diffusivity of silver is $\alpha_{\mathrm{Ag}} = 1.7443 \times 10^{-4}$ m^2/s, while that of Tungsten is $\alpha_{\mathrm{W}} = 6.953 \times 10^{-5}$ m^2/s. The diffusivity ratio of the composite is $\frac{\alpha_{\mathrm{Ag}}}{\alpha_{\mathrm{W}}} = 2.50$. A simple thermal diffusion problem under the imposition of Dirichlet conditions is considered. The steady-state temperature profile, when a constant temperature of 0.5 is maintained on the left wall and a constant temperature of -0.5 is maintained on the right wall, is evaluated. All the other walls are thermally insulated. In the fully-resolved case, the computational domain of $65 \times 65 \times 65$ is discretized using 262,114 uniform hexahedral elements. A time step of $\delta t = 1 \times 10^{-2}$ s is used to solve the fully-resolved problem. The simulation was run for 2000 time steps. The steady state temperature profile in this fully-resolved case is shown in Fig. 6a. This solution is denoted as u^{FEM} and is used in determining the error of the reconstructed VMS solution for different coarse element sizes and varying time steps.

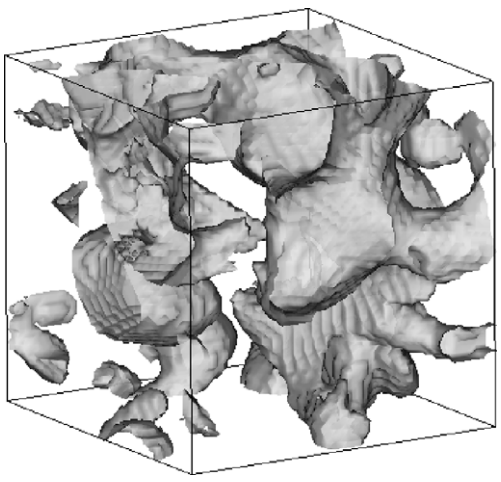

Fig. 5. Schematic of the computational system used for validation of the VMS method.

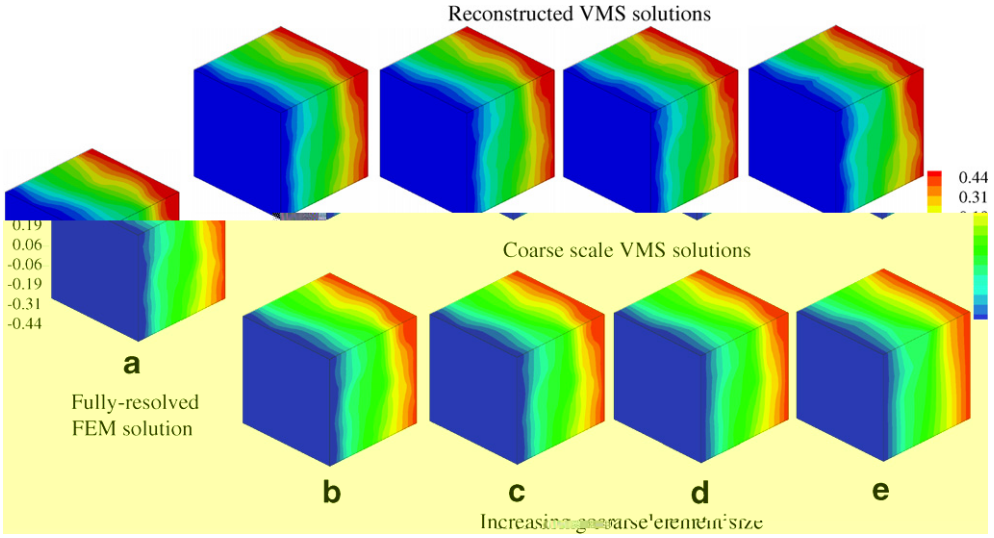

Fig. 6. Comparison of the VMS solution with the fully-resolved solution. (a) Fully-resolved simulation; (Number of elements = 262,114, $\delta t = 1 \times 10^{-2}$) (b)–(e) Top row, Reconstructed VMS solution; Bottom row, corresponding coarse scale VMS solutions. Number of elements used for these simulations (number within brackets is the subgrid discretization) : (b) 32,768 (8), (c) 4096 (64), (d) 512 (512), (e) 64 (4096). The coarse scale time step used in all cases: $\Delta t = 1.0$.

A series of simulations were performed by increasing the size of the coarse element from a size of $2 \times 2 \times 2$ to $32 \times 32 \times 32$ pixels. The total number of elements in the computational domain decreased from 32,768 (for the case when the coarse element is $2 \times 2 \times 2$ pixels) to 8 (for the case when the coarse element is $32 \times 32 \times 32$ pixels). For these problems. the corresponding subgrid discretization varied from $2 \times 2 \times 2$ to $32 \times 32 \times 32$, respectively. The reconstructed solution from each coarse scale discretization is denoted by u^{VMS}. Both the coarse scale and the reconstructed VMS solutions are plotted in Fig. 6b–e. The error is defined as $e = \sqrt{\frac{1}{N_{\mathrm{nodes}}} \sum_{i=1}^{N_{\mathrm{nodes}}} (u_i^{\mathrm{FEM}} - u_i^{\mathrm{VMS}})^2}$. Fig. 7 plots the error for increasing the size of the coarse scale element. Furthermore, another series of simulations were performed by increasing the time step Δt of the VMS solution procedure from the fully resolved transient time step of $\delta t = 1 \times 10^{-2}$ to a time step of $\Delta t = 10$. This set of simulations was performed on a $32 \times 32 \times 32$ discretization of the domain. The subgrid discretization for this problem is $2 \times 2 \times 2$. Fig. 8 plots the error for increasing the size of the time step Δt. A moderate coarse

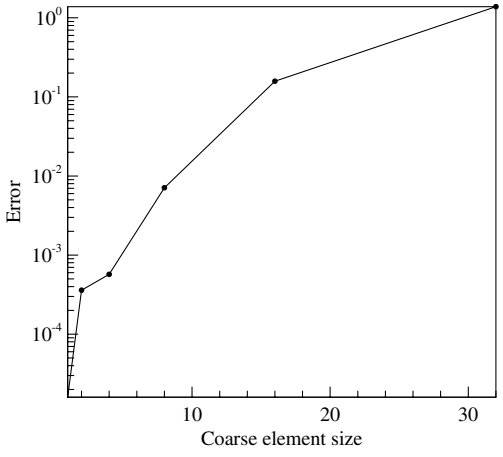

Fig. 7. Error between reconstructed VMS solution and fully-resolved FEM simulation with increasing coarse element size.

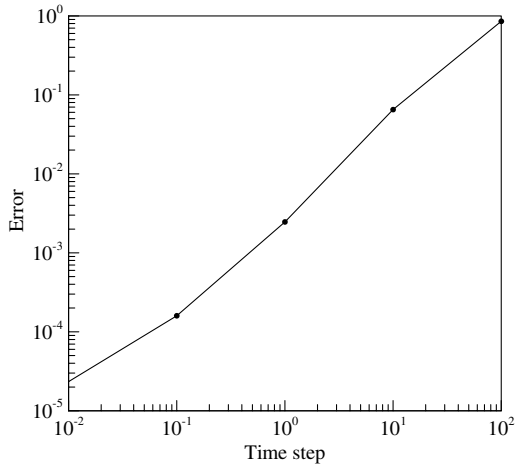

Fig. 8. Error between reconstructed VMS solution and fully-resolved FEM simulation with increasing coarse scale time step Δt.

element size $8 \times 8 \times 8$ and a moderate time step $\Delta t = 1$ result in large computational gains while still resolving the effects of the fine scale.

6.1.3. Constructing the stochastic solution

A simple MATLAB [52] wrapper program was developed that first initializes the stochastic dimensions and constructs the sparse grid coordinates. The corresponding transformed sparse grid coordinates in $\mathscr{H}$ are then estimated. The deterministic VMS code is run for each collocation point and the appropriately named result files are available. The wrapper program then reads the input data and constructs the interpolation function. For the rapid construction of the interpolation functions, we utilize the efficient interpolation toolkit developed by A. Klimle: Sparse grid interpolation toolbox [53,54].

7. Numerical example

In the following section, an illustrative example showcasing the theoretical developments detailed above is provided. We start from a given experimental image. The image (204 μm × 236 μm), shown in Fig. 9, is of a Tungstan-Silver composite (from Umekawa et al. [55]). This composite was produced by infiltrating a porous tungsten solid with molten silver. This is a well characterized system, which has been used to test various reconstruction procedures [42,46].

The first step is to extract the necessary statistical information from the experimental image. The image is cropped, deblurred and discretized. The volume fraction of silver is $p = 0.2$. The experimental two-point

Fig. 9. Experimental image of a two-phase composite (from [55]).

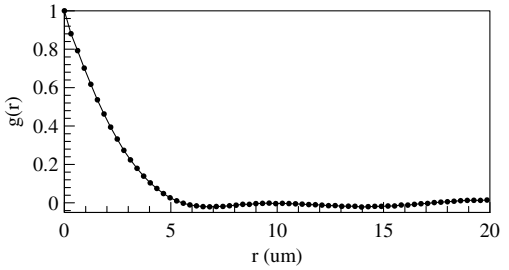

Fig. 10. The two-point correlation function.

correlation is extracted from the image. The normalized two-point correlation $\left(g(r) = \frac{L_2(r)-p^2}{p-p^2}\right)$, is shown in Fig. 10.

The next step is to utilize these extracted statistical relations (volume fraction and two-point correlation) to reconstruct a class of 3D microstructures. We utilize a statistics based reconstruction procedure based on Gaussian Random Fields (GRF). In this method, the 3D microstructure is obtained as the level cuts to a random field. This random field satisfies a given field-field correlation. The statistics of the reconstructed 3D image can be matched to the experimental image by suitably modifying the field-field correlation function and the level cut values (see [42] for a detailed discussion). Following the work of Roberts and Garboczi [42], the GRF is assumed to satisfy a specified field-field correlation given by:

$$\gamma(r) = \frac{e^{-r/\beta} - (r_c/\beta)e^{-r/r_c}}{1-(r_c/\beta)} \frac{\sin(2\pi r/d)}{2\pi r/d}, \tag{57}$$

where the field is characterized by the correlation length β, a domain scale d and a cutoff scale r_c. Optimal values of (β, d, r_c) are obtained by minimizing the error between the theoretical two-point correlation and the experimental two-point correlation. The theoretical two-point correlation corresponding to $(\beta,d,r_c) = (2.229, 12.457, 2.302)$ μm is plotted in Fig. 11.

Using the optimal parameters of the GRF (to match with the experimental data), realizations of 3D microstructure were computed. Each microstructure consisted of $129 \times 129 \times 129$ pixels. This corresponds to a size of 39.7 μm × 39.7 μm × 39.7 μm. One realization of the 3D microstructure reconstructed using the GRF is shown in Fig. 12.

Model reduction based on principle component analysis was implemented using the *eigs* subroutine in Matlab [52]. The implementation of the PCA ensured that these eigen-images are normalized. Principle component analysis of the microstructure dataset revealed that the first 9 eigen-images could represent about 95% of the eigen-spectrum (see Fig. 13). The stochastic dimension is set at $N = 9$.

Microstructures reconstructed using the eigen-images contain fractional values due to the removal of smaller basis components. These fractional pixel values are rounded off to get the digitized microstructure [40,46]. The sequential contraction of $\mathbb{R}^N$ to $\mathscr{H}$ was implemented as a set of Matlab routines. Enforcing the pixel based bounds and the linear equality constraint (of volume fraction) was developed as a convex hull problem.

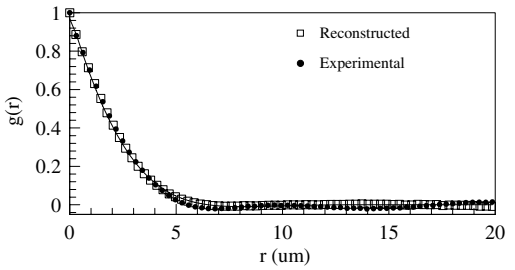

Fig. 11. Comparison of the two-point correlation function from experiments and from the GRF.

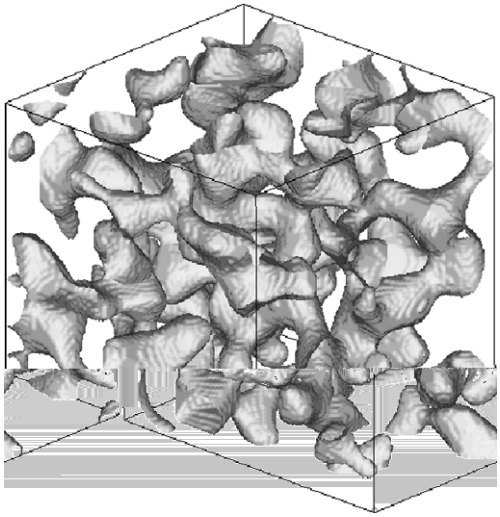

Fig. 12. One instance (realization) of the two-phase microstructure.

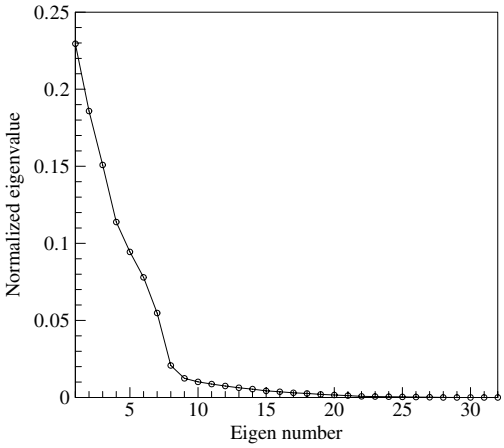

Fig. 13. Eigen-spectrum of the reconstructed microstructural images.

A primal-dual polytope method was employed to construct the set of vertices. Enforcing the second-order constraints was performed through the quadratic programming tools in the optimization toolbox in Matlab. Two separate cases are considered in this example. In the first case, only the first-order constraints (volume fraction) are used to reconstruct the subspace $\mathscr{H}$. In the second case, both first-order as well as second-order constraints (volume fraction and two-point correlation) are used to construct the subspace $\mathscr{H}$.

The above procedure results in the function $\mathscr{G}$. $\mathscr{G}$ is a 9-dimensional function that serves as the stochastic input for the diffusion equation. A simple diffusion problem is considered. A computational domain of $128 \times 128 \times 128$ is considered (this corresponds to a physical domain of $39.7\ \mu m \times 39.7\ \mu m\ \times 39.7\ \mu m$). The random heterogeneous microstructure is constructed as a $129 \times 129 \times 129$ pixel image. The steady-state temperature profile, when a constant temperature of 0.5 is maintained on the left wall and a constant temperature of -0.5 is maintained on the right wall, is evaluated. All the other walls are thermally insulated. The axis along which the temperature boundary conditions are imposed is denoted as the x-axis (left-right) while the vertical axis is the z-axis.

The construction of the stochastic solution is through sparse grid collocation strategies. A level 5 interpolation scheme is used to compute the stochastic solution in 9 dimensions. The stochastic problem was reduced

to the solution of 15713 deterministic decoupled equations. Forty nodes (each with two 3.8G CPUs) of our 64-node Linux cluster were utilized to solve these deterministic equations. These are dual core processors with hyper-threading capabilities thus each node was used to perform the computation for 4 such problems. The total computational time was about 56 h. Each deterministic problem involved the solution of a diffusion problem on a given microstructure using an $8 \times 8 \times 8$ coarse element grid (uniform hexahedral elements) with each coarse element having $16 \times 16 \times 16$ fine-scale elements. The solution of one deterministic VMS problem took about 34 min. In comparison, one fully-resolved deterministic fine scale FEM solution took nearly 40 h

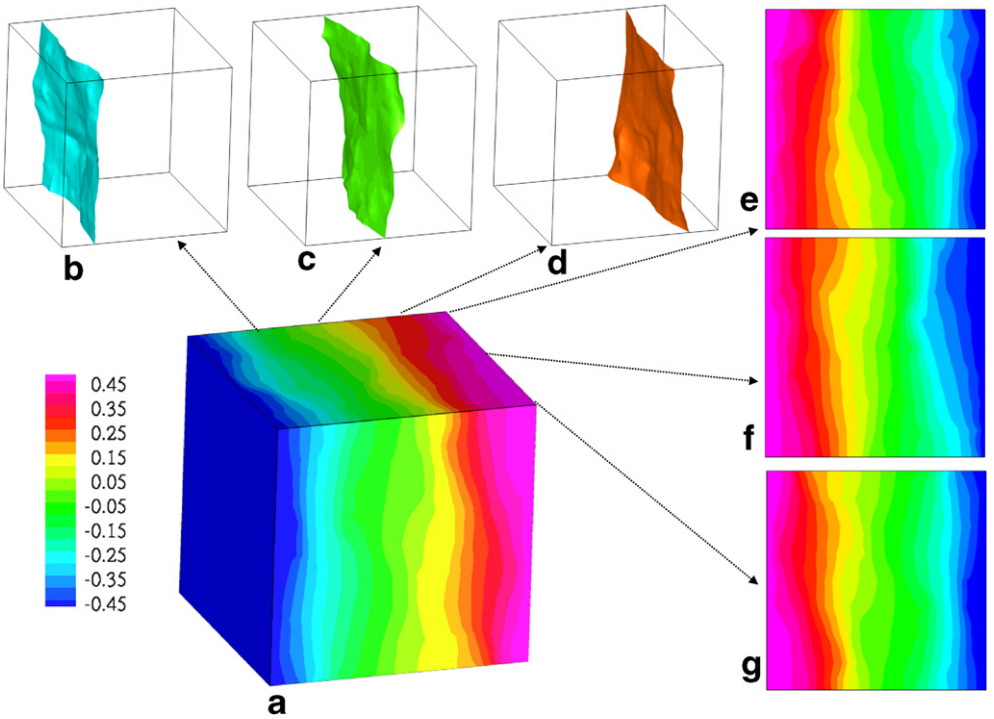

Fig. 14. Steady-state mean temperature (using first-order constraints): (a) temperature contour; (b)–(d) temperature iso-surfaces; (e)–(g) temperature slices.

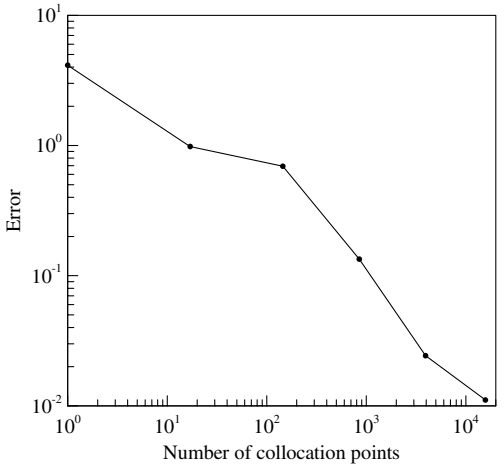

Fig. 15. Reduction in the interpolation error with increasing number of samples (first-order constraint imposed).

on a single processor. This clearly emphasizes the utility of the VMS procedure used here as a purely computational tool (resulting in two orders of reduction in computational effort).

The reduction in the interpolation error with increasing depth of interpolation is shown in Fig. 15. The interpolation error is defined as the variation of the interpolated value of the function from the computed value ($e = \max(|f - I(f)|)$). As the level of interpolation increases, the number of sampling points used to construct the stochastic solution increases (see [26] and [17] for explicit formulae relating the depth of interpolation and the number of sampling points and further related discussions).

The mean temperature for the first case is shown in Fig. 14. The figure plots iso-surfaces of temperatures −0.25 (Fig. 14b), 0.0 (Fig. 14c) and 0.25 (Fig. 14d). The figure also shows temperature slices at three different locations of the xz plane: $y = 0$ (Fig. 14e), $y = 20$ μm (Fig. 14f) and $y = 40$ μm (Fig. 14g).

The standard deviation and other higher-order statistics of the temperature variation are shown in Fig. 16. Fig. 16a plots standard deviation iso-surfaces. Figs. 16d–f plot slices of the temperature deviation at three different planes $y = 0$, $y = 20$ μm, $y = 40$ μm, respectively. The standard deviation reaches 8% of the maximum temperature difference maintained. Two points, one from a region of high-standard deviation ($A = (22.15, 20, 0)$ μm) and another from a region of moderate-deviation ($B = (11.69, 0, 9.23)$ μm), are chosen and the probability distribution functions of temperature at these points determined. Fig. 16b plots the PDF for the point with large standard deviation. Notice that the range of the variability of temperature at this point is rather high.

In the second case, the second-order constraints are also imposed along with the first-order constraints. $g(r)$ at 4 values of r ($r = 5.897$ μm, 6.208 μm, 6.518 μm, 7.139 μm) were enforced to contract the subspace $\mathscr{H}$. A level 5 interpolation scheme in 9 dimensions was used to sample the subspace. The stochastic problem again reduced to the solution of 15,713 deterministic decoupled equations. The interpolation error in this case is plotted in Fig. 17. The mean temperature for this case is shown in Fig. 18. The figure plots iso-surfaces of temperatures −0.25 (Fig. 18b), 0.0 (Fig. 18c) and 0.25 (Fig. 18d). The figure also shows temperature slices at three different locations of the xz plane: $y = 0$ (Fig. 18e), $y = 20$ μm (Fig. 18f) and $y = 40$ μm (Fig. 18g).

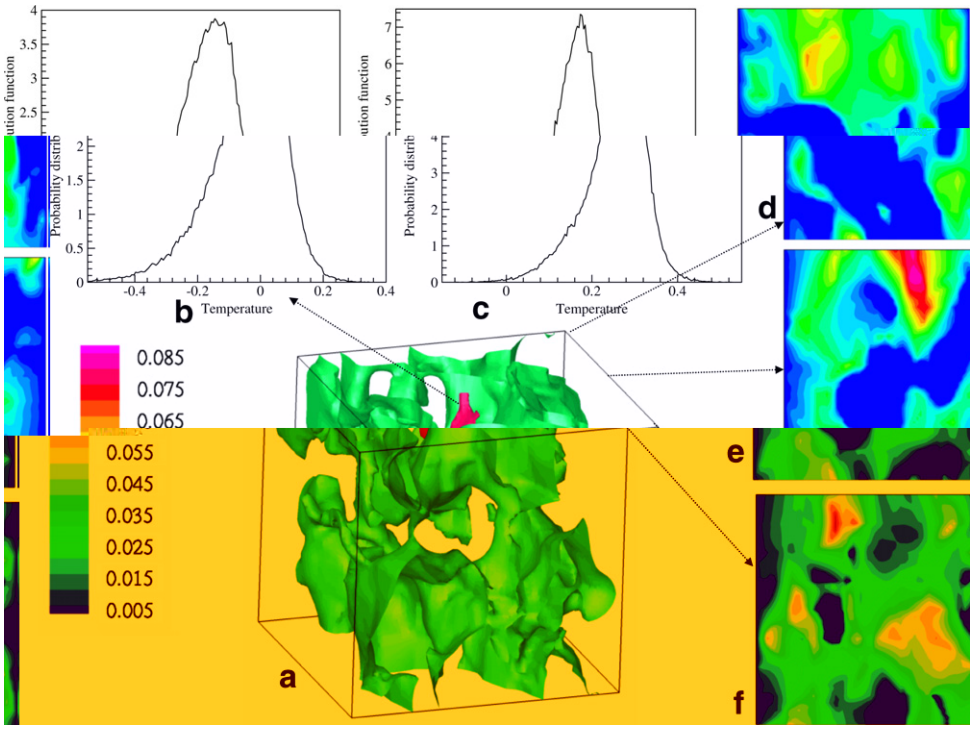

Fig. 16. Standard deviation of temperature (using first-order constraints): (a) standard deviation iso-surfaces; (b,c) temperature PDF at two points. (d)–(f) Standard deviation slices.

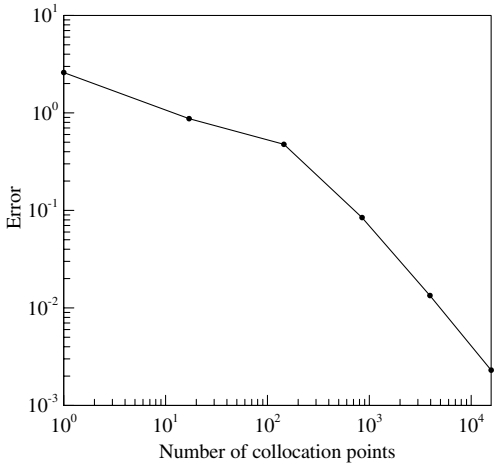

Fig. 17. Reduction in the interpolation error with increasing number of samples (first- and second-order constraints imposed).

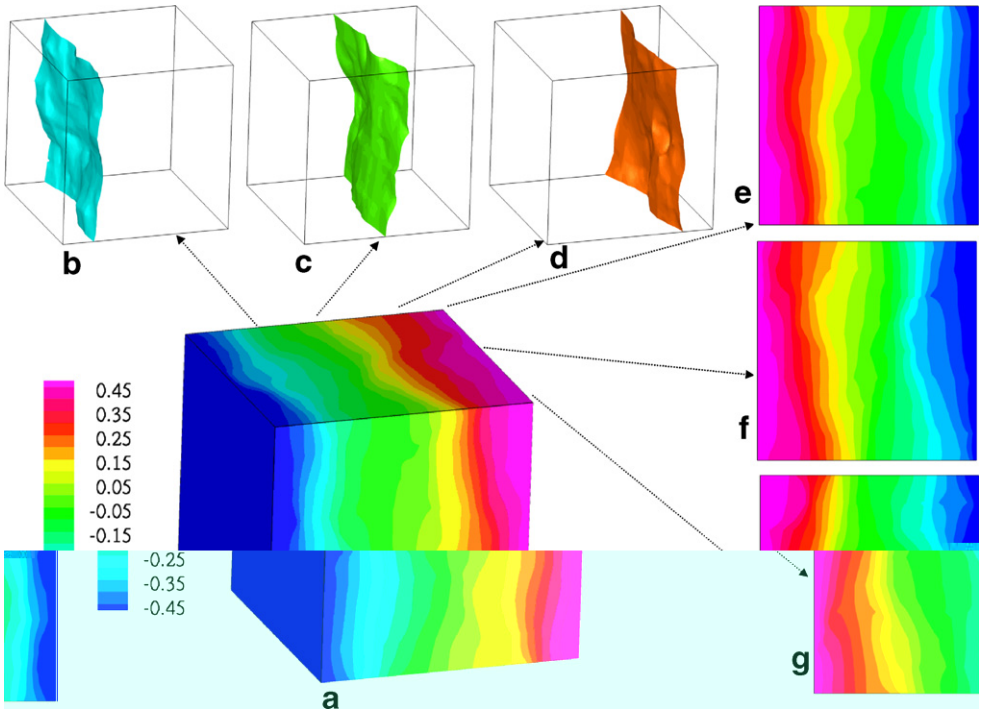

Fig. 18. Steady state mean temperature (using second-order constraints): (a) temperature contour; (b)–(d) temperature iso-surfaces; (e)–(g) temperature slices.

It should be noted that enforcing the second-order constraints only marginally changes the mean temperature profiles (compare the results in Figs. 14 and 18).

The standard deviation and other higher-order statistics of the temperature variation for the second case are shown in Fig. 19. Fig. 19a plots standard deviation iso-surfaces. Notice the reduction in the scale of the variation of the standard deviation. The iso-surfaces of higher variability occupy a much smaller volume due to the enforcement of the second order statistics (compare Fig. 16a and Fig. 19a). Enforcing the second-order constraints causes a large restriction of the allowable space of microstructures.

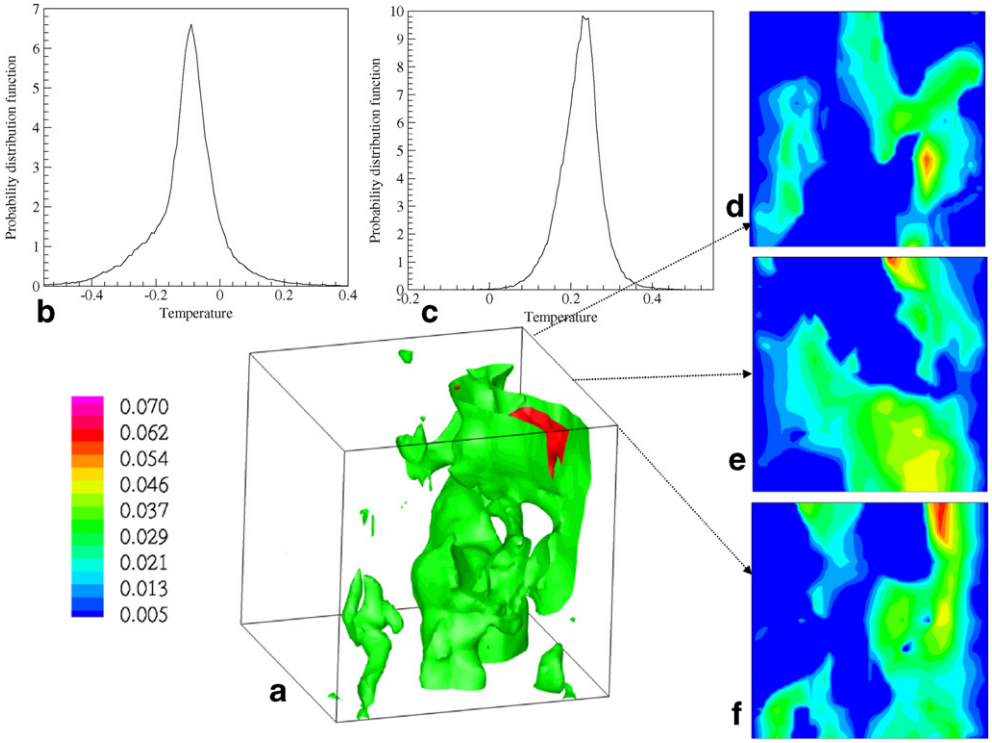

Fig. 19. Standard deviation of temperature (using second-order constraints): (a) standard deviation iso-surfaces; (b,c) temperature PDF at two points. (d)–(f) Standard deviation slices.

Fig. 19d–f plot slices of the temperature deviation at three different planes ($y = 0$ μm, $y = 20$ μm, $y = 40$ μm). The probability distribution functions of temperature at the same points as used in the first-order case are determined. Fig. 19b and c plot the PDF for these points. Notice the reduction in the range of variability of the temperature due to the enforcement of the second-order statistics. This is clearly illustrated in Fig. 20, where the PDFs of the two points are plotted for both the first- and second-order statistics. When only first-order constraints are imposed, the range of variability of the temperature is $[-0.5, 0.45]$, i.e. almost 98% of the whole range of applied temperatures $[-0.5, 0.5]$. When second-order constraints are applied, this range is

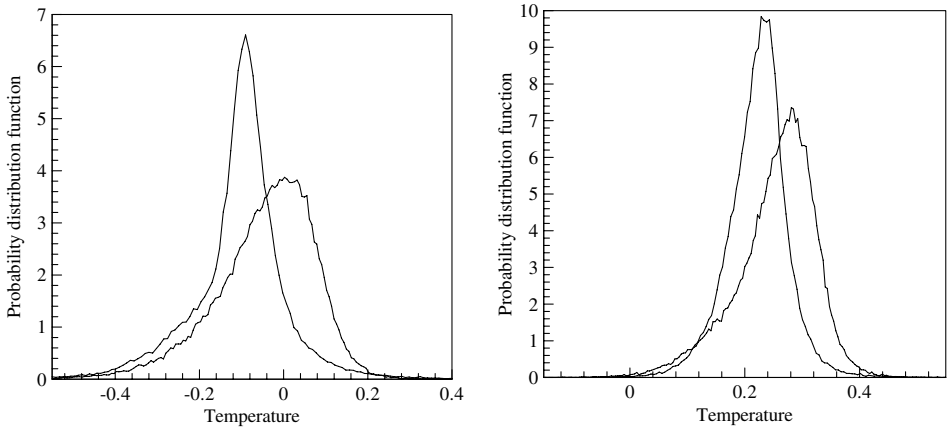

Fig. 20. Comparison of temperature PDFs at two points (left, $A = (22.15, 20, 0)$ μm and right, $B = (11.69, 0, 9.23)$ μm) under the application of first- and second-order constraints.

reduced to about 65% of the applied temperature range. By defining and enforcing higher order statistics at different locations, the subspace $\mathscr{H}$ can be reduced further.

8. Conclusions

We described a novel framework for modeling diffusion in random two-phase media. A general methodology was presented for constructing a reduced-order microstructure model for use as random input in the solution of stochastic partial differential equations governing physical processes (here diffusion) in such media. The reduced-order model is built from reconstructed microstructure images. A sequential process that enforces first, second- and higher-order statistics into the reduced-order model is provided. Two major problems affecting analysis of heterogeneous random media are investigated. The problem of randomness of the microstructure is solved by reformulating the problem as a stochastic differential equation. The recently developed sparse grid stochastic collocation method is used to solve the high-dimensional stochastic problem. The fine length scale variation of the microstructure affects the thermal evolution in the microstructure. A computation technique (VMS) to incorporate the fine scale effects into the coarse scale solution is used. An illustrative example is presented to demonstrate the ability of the methodology to compute at each point within the microstructure the probability distribution of fields (e.g. temperature) as a result of microstructural (and corresponding property) randomness. The effect of incorporating higher-order statistics is clearly seen.

We are currently investigating different aspects of the problems examined here, namely: using more sophisticated model reduction techniques to build the reduced-order microstructure model, extending the methodology to arbitrary types of microstructures as well as developing models of advection-diffusion in random heterogeneous media. In addition to the importance of such models in process modeling of heterogeneous materials (polycrystals, composites, concrete, etc.), many other technological applications in modeling multiscale thermal/flow transport in geological media, soil contamination and reservoir engineering remain to be explored.

Acknowledgements

This research was supported by the Computational Mathematics program of AFOSR (Grant F49620-00-1-0373). The computing was conducted using the resources of the Cornell Theory Center, which receives funding from Cornell University, New York State, federal agencies, and corporate partners.

References

[1] G.M. Homsy, Viscous fingering in porous media, Ann. Rev. Fluid. Mech. 19 (1987) 271–311.
[2] T. Arbogast, S.L. Bryant, A two-scale numerical subgrid technique for waterflood simulations, SPE J. (2002) 446–457.
[3] T.J.R. Hughes, Multiscale phenomena: Green's functions, the Dirichlet-to-Neumann formulation, subgrid scale models, bubbles and the origin of stabilized methods, Comp. Meth. Appl. Mech. Eng. 127 (1995) 387–401.
[4] W.E.B. Engquist, The heterogeneous multiscale methods, Comm. Math. Sci. 1 (1) (2003) 87–133.
[5] P.B. Ming, P.W. Zhang, Analysis of the heterogeneous multiscale method for elliptic homogenization problems, preprint, 2003.
[6] T.Y. Hou, X.H. Wu, A multiscale finite element method for elliptic problems in composite materials and porous media, J. Comput. Phys. 134 (1997) 169–189.
[7] I. Babuska, U. Banerjee, J. Osborn, Generalized finite element methods: main ideas, results and perspective, Int. J. Comput. Meth. 1 (2004) 67–103.
[8] G. Sangalli, Capturing small scales in elliptic problems using a residual-free bubbles finite element method, SIAM MMS 1 (2003) 485–503.
[9] R.G. Ghanem, P.D. Spanos, Stochastic Finite Elements: A Spectral Approach, Dover Publications, 1991.
[10] R. Ghanem, Probabilistic characterization of transport in heterogeneous porous media, Comput. Methods Appl. Mech. Eng. 158 (1998) 199–220.
[11] R. Ghanem, A. Sarkar, Mid-frequency structural dynamics with parameter uncertainty, Comput. Methods Appl. Mech. Eng. 191 (2002) 5499–5513.
[12] D. Xiu, G.E. Karniadakis, Modeling uncertainty in steady state diffusion problems via generalized polynomial chaos, Comput. Methods Appl. Mech. Eng. 191 (2002) 4927–4948.
[13] D. Xiu, G.E. Karniadakis, Modeling uncertainty in flow simulations via generalized polynomial chaos, J. Comp. Phys. 187 (2003) 137–167.

[14] I. Babuska, R. Tempone, G.E. Zouraris, Solving elliptic boundary value problems with uncertain coefficients by the finite element method: the stochastic formulation, Comput. Methods Appl. Mech. Eng. 194 (2005) 1251–1294.
[15] I. Babuska, R. Tempone, G.E. Zouraris, Galerkin finite elements approximation of stochastic finite elements, SIAM J. Numer. Anal. 42 (2004) 800–825.
[16] D. Xiu, D. Lucor, C.-H. Su, G.E. Karniadakis, Performance evaluation of generalized polynomial chaos, in: International Conference on Computational Science, Lecture Notes in Computer Science, vol. 2660, Springer, 2003, pp. 346–354.
[17] B. Ganapathysubramanian, N. Zabaras, Sparse grid collocation schemes for stochastic natural convection problems, J. Comp. Physics (2007), doi:10.1016/j.jcp.2006.12.014.
[18] D. Xiu, J.S. Hesthaven, High-order collocation methods for the differential equation with random inputs, SIAM J. Sci. Comput. 27 (2005) 1118–1139.
[19] D. Xiu, Efficient collocational approach for parametric uncertainty analysis, Comm. Comput. Phys. 2 (2) (2007) 293–309.
[20] X. Wan, G.E. Karniadakis, An adaptive multi-element generalized polynomial chaos method for stochastic differential equations, J. Comp. Phys. 209 (2005) 617–642.
[21] B. Velamur Asokan, N. Zabaras, Using stochastic analysis to capture unstable equilibrium in natural convection, J. Comp. Phys. 208 (2005) 134–153.
[22] I. Babuska, F. Nobile, R. Tempone, A stochastic collocation method for elliptic partial differential equations with random input data, ICES Report 05-47, 2005.
[23] F. Nobile, R. Tempone, C.G. Webster, A sparse grid stochastic collocation method for elliptic partial differential equations with random input data, preprint.
[24] T. Gerstner, M. Griebel, Numerical integration using sparse grids, Numer. Algor. 18 (1998) 209–232.
[25] V. Barthelmann, E. Novak, K. Ritter, High-dimensional polynomial interpolation on sparse grids, Adv. Comput. Math. 12 (2000) 273–288.
[26] A. Klimke, Uncertainty Modeling using Fuzzy Arithmetic and Sparse Grids, PhD Thesis, Universität Stuttgart, Shaker Verlag, Aachen, 2006.
[27] B. Velamur Asokan, N. Zabaras, A stochastic variational multiscale method for diffusion in random heterogeneous media, J. Comp. Phys. 218 (2006) 654–676.
[28] D. Xiu, D.M. Tartakovsky, A two-scale non-perturbative approach to uncertainty analysis of diffusion in random composites, SIAM J. Multiscale Model. Simul. 2 (2004) 662–674.
[29] A. Doostan, R. Ghanem, On the construction and analysis of stochastic models: characterization and propagation of the errors associated with limited data, J. Comp. Phys. 217 (2006) 63–81.
[30] L. Guadagnini, A. Guadagnini, D.M. Tartakovsky, Probabilistic reconstruction of geologic facies, J. Hydrol. 294 (2004) 57–67.
[31] C.L. Winter, D.M. Tartakovsky, Mean flow in composite porous media, Geophys. Res. Lett. 27 (2000) 1759–1762.
[32] C.L. Winter, D.M. Tartakovsky, Groundwater flow in heterogeneous composite aquifers, Water Resour. Res. 38 (2002) 23.1–23.11.
[33] C. Desceliers, R. Ghanem, C. Soize, Maximum likelihood estimation of stochastic chaos representations from experimental data, Int. J. Numer. Meth. Eng. 66 (2006) 978–1001.

[50] V. Sundararaghavan, N. Zabaras, Classification of three-dimensional microstructures using support vector machines, Comp. Mat. Sci. 32 (2005) 223–239.
[51] J. Nocedal, S.J. Wright, Numerical Optimization, Springer-Verlag, 2000.
[52] <http://www.mathworks.com/products/matlab/>.
[53] A. Klimke, B. Wohlmuth, Algorithm 847: *spinterp*: Piecewise Multilinear Hierarchical Sparse Grid Interpolation in *MATLAB*, ACM Transactions on Mathematical Software 31 (2005).
[54] A. Klimke, Sparse Grid Interpolation Toolbox – User's Guide, IANS Report 2006/001, University of Stuttgart, 2006.
[55] S. Umekawa, R. Kotfila, O.D. Sherby, Elastic properties of a tungsten–silver composite above and below the melting point of silver, J. Mech. Phys. Solids 13 (1965) 229–230.